Available online at www.sciencedirect.com
ScienceDirect
Comput. Methods Appl. Mech. Engrg. 374 (2021) 113562
Computer methods in applied mechanics and engineering
www.elsevier.com/locate/cma

Mixed Kirchhoff stress–displacement–pressure formulations for incompressible hyperelasticity

Patrick E. Farrell[a], Luis F. Gatica[b,c], Bishnu P. Lamichhane[d], Ricardo Oyarzúa[e,c], Ricardo Ruiz-Baier[f,*]

[a] *Mathematical Institute, University of Oxford, Andrew Wiles Building, Woodstock Road, Oxford OX2 6GG, UK*
[b] *Departamento de Matemática y Física Aplicadas, Universidad Católica de la Santísima Concepción, Casilla 297, Concepción, Chile*
[c] *CI²MA, Universidad de Concepción, Chile*
[d] *School of Mathematical and Physical Sciences, The University of Newcastle, Callaghan, NSW 2308, Australia*
[e] *GIMNAP, Departamento de Matemática, Universidad del Bío-Bío, Concepción, Chile*
[f] *School of Mathematics, Monash University, 9 Rainforest Walk, Clayton, Victoria 3800, Australia*

Received 1 July 2020; received in revised form 24 September 2020; accepted 5 November 2020
Available online xxxx

Abstract

The numerical approximation of hyperelasticity must address nonlinear constitutive laws, geometric nonlinearities associated with large strains and deformations, the imposition of the incompressibility of the solid, and the solution of large linear systems arising from the discretisation of 3D problems in complex geometries. We adapt the three-field formulation for nearly incompressible hyperelasticity introduced in Chavan et al. (2007) to the fully incompressible case. The mixed formulation is of Hu–Washizu type and it differs from other approaches in that we use the Kirchhoff stress, displacement, and pressure as principal unknowns. We also discuss the solvability of the linearised problem restricted to neo-Hookean materials, illustrating the interplay between the coupling blocks. We construct a family of mixed finite element schemes (with different polynomial degrees) for simplicial meshes and verify its error decay through computational tests. We also propose a new augmented Lagrangian preconditioner that improves convergence properties of iterative solvers. The numerical performance of the family of mixed methods is assessed with benchmark solutions, and the applicability of the formulation is further tested in a model of cardiac biomechanics using orthotropic strain energy densities. The proposed methods are advantageous in terms of physical fidelity (as the Kirchhoff stress can be approximated with arbitrary accuracy and no locking is observed) and convergence (the discretisation and the preconditioners are robust and computationally efficient, and they compare favourably at least with respect to classical displacement–pressure schemes).

MSC: 35Q74; 65N60; 74B20; 65F99

Keywords: Kirchhoff stress formulation; Incompressible hyperelasticity; Augmented Lagrangian preconditioning; Mixed finite element methods

* Corresponding author.
E-mail addresses: patrick.farrell@maths.ox.ac.uk (P.E. Farrell), lgatica@ucsc.cl (L.F. Gatica), bishnu.lamichhane@newcastle.edu.au (B.P. Lamichhane), royarzua@ubiobio.cl (R. Oyarzúa), ricardo.ruizbaier@monash.edu (R. Ruiz-Baier).

https://doi.org/10.1016/j.cma.2020.113562
0045-7825/

1. Introduction

Mixed methods for nonlinear solid mechanics consider additional fields in the variational formulation, minimising suitable energy functionals and using further constraints. Approaches based on the Hu–Washizu and Hellinger–Reissner principles are among the most popular choices, and they often lead to saddle-point problems where suitable inf–sup conditions need to be satisfied (see, e.g., [1,2]). Recent variants of these methods include mixed (first Piola–Kirchhoff) stress tensor and displacement formulations, introduced in [3], and arising from inversion of the constitutive relations; or assumed stress and similar approaches [4,5]. Also, a hybridisable discontinuous Galerkin method based on the minimisation of the potential energy has been analysed in [6], where the authors also discuss scenarios where the convergence is compromised, and propose a stabilisation strategy. Mixed formulations involving pseudo-stress, displacement and pressure have been studied in [7]. Recent comparisons between different discontinuous approximations can be found in [8] and between least-squares mixed formulations in [9].

Mixed finite element methods are a natural remedy for schemes based on primal formulations that are prone to poor performance and numerical artefacts for bending dominated and nearly incompressible regimes (in the sense that the computational results can differ substantially from what is expected from the physical and mathematical structure of the problem [10]), but other approaches also are available to improve the approximation of large deformation problems. These alternatives include high-order pure displacement methods designed to be robust in the nearly incompressible limit [11], reduced and selective integration [12], nonconforming displacement–pressure [13], generalised schemes [14], projection methods [15], enhanced strain [16,17], methods based on biorthogonal systems [18] or extended finite element approaches [19] (see also the general monographs and reviews in [1,20,21]).

More pertinent to the present case, formulations in terms of Kirchhoff stress, displacement and pressure were introduced in [22] and have been adapted to the study of cardiac electromechanics in [23,24]. Recasting the three-field formulation in this particular set of unknowns is very useful for modelling the physiological responses of cardiac tissue, as the Kirchhoff stress tensor acts as the coupling field with the equations describing electrical propagation in stress-assisted diffusion models. It thus allows for the direct approximation of the variables of interest [24]. An additional key feature is that the formulation imposes symmetry of the stress without the need for additional reconstruction or complicated element choices. This approach is more efficient and natural than a mixed finite element method based on weakly imposed symmetry for the stress [25,26], where an additional constraint should be introduced to impose the symmetry of the stress.

Solving the three-field formulation using a suitable discretisation also avoids volumetric locking. However, the size of the systems involved leads to rather high computational costs, thus making the adoption of robust and efficient iterative solvers important. Apart from the references mentioned above, we stress that within the context of cardiac mechanics, the present contribution complements the works defining strain-based formulations [27], stabilised formulations [28,29], displacement–pressure discontinuous Galerkin [30], and pure displacement [31–34] methods. In clinically-oriented applications, the performance of numerical solvers is particularly crucial. The primary difficulties not only lie with the high spatial and temporal resolutions required by the simulations of patient-specific physiological conditions, but also with the time constraints posed by clinical diagnosis. As a result, the use of preconditioning techniques is mandatory for lowering the computational cost associated with diagnostic-oriented simulations. Some preconditioners tailored for achieving robustness in the numerical approximation of hyperelasticity of soft tissue have been advanced recently in [35–37]. They consist of augmented Lagrangian type, of nested block factorisation decoupling mass from momentum balances, and of splitting the system matrix into a small block and a series of multigrid solves, respectively.

Let us recall that (left) preconditioning improves the spectral properties of a general linear system [38] by pre-multiplying both sides of the equation with a matrix $\mathcal{P}^{-1}$:

$$\begin{aligned} &\mathcal{A}u = b \\ \Longrightarrow\ &\mathcal{P}^{-1}\mathcal{A}u = \mathcal{P}^{-1}b. \end{aligned}$$

Roughly speaking, the quality of a preconditioner depends on how closely $\mathcal{P}^{-1}$ can approximate the exact inverse of $\mathcal{A}$; the better the approximation, the higher the quality [39]. The choice of $\mathcal{P}^{-1}$ for block systems relies heavily on knowledge about the block structure of $\mathcal{A}$. For a general non-singular 2×2 block matrix with a non-singular top-left block A,

$$\mathcal{A} = \begin{bmatrix} A & B \\ C & D \end{bmatrix}, \tag{1.1}$$

a popular class of preconditioners builds on the block factorisation formula [38,40–43]

$$\mathcal{A}^{-1} \approx \mathcal{P}^{-1} = \begin{bmatrix} I & -\hat{A}^{-1}B \\ 0 & I \end{bmatrix} \begin{bmatrix} \hat{A}^{-1} & 0 \\ 0 & \hat{S}^{-1} \end{bmatrix} \begin{bmatrix} I & 0 \\ -C\hat{A}^{-1} & I \end{bmatrix},$$

where $\hat{A}^{-1}$ and $\hat{S}^{-1}$ are respectively approximations of A^{-1} and S^{-1}, with $S = D - CA^{-1}B$ being the Schur complement in (1.1). It is important to point out that in the context of the proposed formulation for hyperelasticity, A acts on the displacement and Kirchhoff stress, while D acts on the pressure. Interpreting the inverse of a matrix as the action of solving a linear system involving the original matrix, this block Gaussian elimination then reduces the problem of solving the coupled preconditioned system to that of solving two separate smaller linear systems involving matrices $\hat{A}$ and $\hat{S}$. As a result, the availability of fast approximate solvers for the two smaller linear problems is crucial to the performance of the preconditioner.

Even if a robust approximation for the top-left block A is known, approximating the Schur complement S is usually a challenging task, as it is typically dense [44]. An augmented Lagrangian approach which effectively controls the Schur complement for the Oseen problem was introduced in [44]. The idea is to introduce an extra term in the variational formulation that does not affect the overall continuous solution, but serves to ease the approximation of the Schur complement [45]. This extra augmentation is weighted by a positive constant γ, and is often regarded as the penalty term enforcing the constraint in the problem. Adding the augmented term leads to changes in the linear system, in particular changes to the blocks of the matrix $\mathcal{A}$, with $\hat{A}_\gamma$ and $\hat{S}_\gamma$ being the augmented versions of $\hat{A}$ and $\hat{S}$; by increasing the penalty parameter γ, $\hat{S}_\gamma$ becomes a better and better approximation to S_γ, at the cost of making the operator A_γ more complex. In our context, the augmented Lagrangian strategy allows us to apply direct factorisations to A_γ instead of $\mathcal{A}$, substantially decreasing time to solution.

The outline of the paper is as follows. Section 2 summarises the equations of hyperelasticity for general constitutive laws, and presents the continuous form of the three-field version of the problem in strong and weak forms. In Section 3 we address the linearisation of the weak form and sketch its solvability analysis when restricted to neo-Hookean materials. There we also discuss the minimisation of the general nonlinear variational form. A mixed finite element discretisation and the construction of an augmented Lagrangian preconditioner are detailed in Section 4. We numerically examine the properties of the formulation, the finite element scheme, and of the preconditioner in Section 5. We conclude in Section 6 with a brief summary of our findings and also discussing ongoing extensions of this work.

2. Model description

2.1. Kinematics and constitutive relations

Let $\Omega \subset \mathbb{R}^d$ ($d \in \{2, 3\}$) denote an open, connected Lipschitz domain with piecewise smooth boundary $\partial\Omega$, representing the shape and position of a deformable body in its stress-free reference configuration, and denote by $\boldsymbol{n}$ the outward unit normal vector on $\partial\Omega$. The kinematic description of finite deformations is made precise as follows. A material point in Ω is denoted by $\boldsymbol{x}$, whereas $\mathbf{U} : \Omega \to \mathbb{R}^d$ will denote the displacement field defining its new position $\boldsymbol{x} + \mathbf{U}(\boldsymbol{x})$ in the deformed configuration. The tensor $\mathbf{F} := \mathbf{I} + \nabla\mathbf{U}$ is the gradient (applied with respect to the fixed material coordinates) of the deformation map; its Jacobian determinant, denoted by $J = \det\mathbf{F} = \det(\mathbf{I} + \nabla\mathbf{U})$, measures the solid volume change during the deformation (where $\mathbf{I}$ denotes the second-order identity tensor); and $\mathbf{C} = \mathbf{F}^{\mathrm{t}}\mathbf{F}$ is the right Cauchy–Green deformation tensor on which all strain measures will be based (here the superscript $(\cdot)^{\mathrm{t}}$ denotes the transpose operator). The triplet $(\boldsymbol{f}_0(\boldsymbol{x}), \boldsymbol{s}_0(\boldsymbol{x}), \boldsymbol{n}_0(\boldsymbol{x}))$ represents a coordinate system pointing in the local preferential directions of motion with $\boldsymbol{n}_0(\boldsymbol{x}) = \boldsymbol{f}_0(\boldsymbol{x}) \times \boldsymbol{s}_0(\boldsymbol{x})$, and the system is restricted to $(\boldsymbol{f}_0(\boldsymbol{x}), \boldsymbol{s}_0(\boldsymbol{x}))$ in 2D. The first isotropic invariant ruling deviatoric effects is $I_1(\mathbf{C}) = \mathbf{tr}\mathbf{C}$, and for generic unit vectors $\boldsymbol{f}_0, \boldsymbol{s}_0$, the scalars $I_{4,f}(\mathbf{C}) = \boldsymbol{f}_0 \cdot (\mathbf{C}\boldsymbol{f}_0)$, $I_{4,s}(\mathbf{C}) = \boldsymbol{s}_0 \cdot (\mathbf{C}\boldsymbol{s}_0)$, $I_{8,fs}(\mathbf{C}) = \boldsymbol{f}_0 \cdot (\mathbf{C}\boldsymbol{s}_0)$ are direction-dependent pseudo-invariants of $\mathbf{C}$ measuring direction-specific stretches.

Constitutive relations depend on the specific material under consideration and they are encoded through a strain energy density function Ψ (defined per unit volume in the reference configuration and representing the work per unit reference volume done by the stress in deforming the material system) written solely in terms of the deformation gradient. We consider two cases: the generic neo-Hookean material law and the Holzapfel–Ogden law specifically

designed for orthotropic myocardial tissue [46]. The strain energy densities read respectively

$$\Psi_{\mathrm{NH}}(\mathbf{F}) = \frac{\mu}{2}(I_1 - d), \quad \Psi_{\mathrm{HO}}(\mathbf{F}) = \frac{a}{2b}e^{b(I_1-d)} + \frac{a_{fs}}{2b_{fs}}\left[e^{b_{fs}I_{8,fs}^2} - 1\right] + \sum_{i\in\{f,s\}}\frac{a_i}{2b_i}\left[e^{b_i(I_{4,i}-1)_+^2} - 1\right], \tag{2.1}$$

where μ, a, b, a_i, b_i with $i \in \{f, s, fs\}$ are material parameters and we have used the notation $(s)_+ := s$ if $s > 0$ or zero otherwise. Both specifications in (2.1) satisfy the condition of polyconvexity needed for minimisers of the free potential energy form of the problem to exist [47].

The first Piola–Kirchhoff stress tensor is

$$\mathbf{P} = \frac{\partial \Psi}{\partial \nabla \mathbf{U}} - P(\mathbf{I} + \nabla \mathbf{U})^{-\mathrm{t}}, \tag{2.2}$$

where P denotes the solid hydrostatic pressure, which is the Lagrange multiplier used to impose the incompressibility constraint in the finite strain regime, given by

$$\det(\mathbf{I} + \nabla \mathbf{U}) = 1,$$

and which implies that J does not appear in (2.2). The symmetric Kirchhoff stress tensor (also referred to as effective Kirchhoff stress) is given by

$$\boldsymbol{\Pi} = \mathbf{P}\mathbf{F}^{\mathrm{t}} = \frac{\partial \Psi}{\partial \nabla \mathbf{U}}(\mathbf{I} + \nabla \mathbf{U})^{\mathrm{t}} - P\mathbf{I}. \tag{2.3}$$

2.2. Force balance and boundary conditions

The constitutive relation, the balance of linear momentum, and the incompressibility constraint are then combined (when posed in the inertial reference frame and under the static mechanical equilibrium configuration) in the following strong form

$$\boldsymbol{\Pi} - \frac{\partial \Psi}{\partial \nabla \mathbf{U}}(\mathbf{I} + \nabla \mathbf{U})^{\mathrm{t}} + P\mathbf{I} = \mathbf{0} \qquad \text{in } \Omega, \tag{2.4a}$$

$$-\mathbf{div}\, \boldsymbol{\Pi}(\mathbf{I} + \nabla \mathbf{U})^{-\mathrm{t}} = \rho_0 \boldsymbol{b} \qquad \text{in } \Omega, \tag{2.4b}$$

$$\det(\mathbf{I} + \nabla \mathbf{U}) - 1 = 0 \qquad \text{in } \Omega, \tag{2.4c}$$

where ρ_0 is the reference medium density and $\boldsymbol{b}$ is a vector field of body loads (body force per unit undeformed volume). The balance of angular momentum translates into the condition of symmetry of the Kirchhoff stress tensor and it is implicitly carried by the momentum and constitutive relations.

The governing equations (2.4) will be supplemented with mixed displacement and traction boundary conditions

$$\mathbf{U} = \mathbf{0} \quad \text{on} \quad \partial\Omega_D, \qquad \text{and} \qquad \boldsymbol{\Pi}(\mathbf{I} + \nabla \mathbf{U})^{-\mathrm{t}}\boldsymbol{n} = \boldsymbol{t} \quad \text{on} \quad \partial\Omega_N, \tag{2.5}$$

where $\partial\Omega_D$, $\partial\Omega_N$ are a disjoint partition of the boundary $\partial\Omega$ and $\boldsymbol{t}$ is a prescribed traction. We assume that both $\boldsymbol{b}$ and $\boldsymbol{t}$ are sufficiently regular.

2.3. Three-field weak formulation

We proceed to test (2.4a)–(2.4c) against suitable functions, integrating by parts only in (2.4b), and using (2.5), to obtain the following nonlinear variational problem: Find $(\boldsymbol{\Pi}, \mathbf{U}, P) \in \mathbb{L}^4_{\mathrm{sym}}(\Omega) \times \mathbf{W}^{1,4}_D(\Omega) \times \mathrm{L}^4(\Omega)$ such that

$$\int_\Omega \left[\boldsymbol{\Pi} - \frac{\partial \Psi}{\partial \nabla \mathbf{U}}(\mathbf{I} + \nabla \mathbf{U})^{\mathrm{t}} + P\mathbf{I}\right] : \boldsymbol{\tau} = 0 \qquad \forall \boldsymbol{\tau} \in \mathbb{L}^4_{\mathrm{sym}}(\Omega), \tag{2.6a}$$

$$\int_\Omega \boldsymbol{\Pi}(\mathbf{I} + \nabla \mathbf{U})^{-\mathrm{t}} : \nabla \boldsymbol{v} = \int_\Omega \rho_0 \boldsymbol{b} \cdot \boldsymbol{v} + \int_{\partial\Omega_N} \boldsymbol{t} \cdot \boldsymbol{v} \qquad \forall \boldsymbol{v} \in \mathbf{H}^1_D(\Omega), \tag{2.6b}$$

$$\int_\Omega [\det(\mathbf{I} + \nabla \mathbf{U}) - 1]\, q = 0 \qquad \forall q \in \mathrm{L}^4(\Omega), \tag{2.6c}$$

where $\mathbb{L}^4_{\mathrm{sym}}(\Omega) := \{\boldsymbol{\tau} \in \mathbb{L}^4(\Omega) : \boldsymbol{\tau} = \boldsymbol{\tau}^{\mathrm{t}}\}$, $\mathbf{W}^{1,4}_D(\Omega) = \{\boldsymbol{v} \in \mathbf{W}^{1,4}(\Omega) : \boldsymbol{v} = \mathbf{0} \text{ on } \partial\Omega_D\}$, and $\mathbf{H}^1_D(\Omega) = \{\boldsymbol{v} \in \mathbf{H}^1(\Omega) : \boldsymbol{v} = \mathbf{0} \text{ on } \partial\Omega_D\}$. We have taken the usual notation for tensor–tensor scalar product $\boldsymbol{\sigma} : \boldsymbol{\tau} = \mathbf{tr}(\boldsymbol{\sigma}^{\mathrm{t}}\boldsymbol{\tau})$, and

we are implicitly assuming that the displacements are admissible in the sense that they have sufficient regularity as made precise above, or they are in $\mathbf{W}^{1,d}(\Omega)$ and they satisfy $\det(\mathbf{I}+\nabla\mathbf{U})>0$ (which implies that deformations are continuous), see e.g. [48–50]. Such regularity for the displacement implies in particular that the integral in the left-hand side of (2.6b) is well-defined when the trial stress and test displacement belong to the spaces mentioned above.

The motivation for using three-field elasticity formulations is to avoid volumetric locking [18], and to provide direct approximation of a variable of importance [23,24], nonetheless at a higher computational cost. As mentioned in [7], capturing stress concentrations with the guarantee of stress convergence under mesh refinement is a key requirement that is very difficult to achieve in a point-wise manner simply by standard displacement-based formulations. A further advantage of using the Kirchhoff stress is that this tensor is symmetric and for simpler material laws is a polynomial function of the displacement gradient, whereas first and second Piola–Kirchhoff stresses are rational functions of it [22]. Existence of minimisers of the elastic energy in a given product space $\vec{E}$ is not guaranteed in general. One can however assume growth conditions on Ψ and that the initial data maintains the material in the hyperelastic range, in such a way that the product space $\mathbb{L}^4_{\mathrm{sym}}(\Omega)\times\mathbf{W}^{1,4}_D(\Omega)\times\mathrm{L}^4(\Omega)$ is contained in $\vec{E}$ [51] (see also [28]). This is discussed further in what follows.

2.4. Energy minimisation and an augmented Lagrangian form

Regarding the general case of nonlinear elasticity, let us denote by $\mathbb{M}^3$ the set of all 3×3 matrices, and

$$\mathbb{M}^3_+=\{\mathbf{A}\in\mathbb{M}^3:\det(\mathbf{A})>0\}.$$

A stored energy function $\Psi:\mathbb{M}^3_+\to\mathbb{R}$ is said to be polyconvex if there exists a convex function $G:\mathbb{M}^3\times\mathbb{M}^3\to\mathbb{R}$ such that

$$\Psi(\mathbf{F})=G(\mathbf{F},\operatorname{adj}\mathbf{F}),\quad \mathbf{F}\in\mathbb{M}^3_+.$$

The function G is coercive if there exist $a\in\mathbb{R}$, $b>0$, $p\geq 2$, and $q\geq\frac{p}{p-1}$ such that

$$G(\mathbf{F},\mathbf{H})\geq a+b(\|\mathbf{F}\|^p+\|\mathbf{H}\|^q),\quad (\mathbf{F},\mathbf{H})\in\mathbb{M}^3\times\mathbb{M}^3,$$

where $\|\mathbf{F}\|$ is the Euclidean norm of the matrix $\mathbf{F}\in\mathbb{R}^{3\times 3}$.

According to the right-hand side of (2.6b), let the linear functional M be defined by

$$M(\boldsymbol{v})=\int_\Omega\rho_0\boldsymbol{b}\cdot\boldsymbol{v}+\int_{\partial\Omega_N}\boldsymbol{t}\cdot\boldsymbol{v},$$

which gives the contribution to the potential energy that corresponds to external applied body and surface loads in the system. Recall that the standard energy approach for nonlinear elasticity is to find the solution of the minimisation problem

$$\frac{1}{2}\int_\Omega\Psi(\mathbf{I}+\nabla\mathbf{U})-M(\mathbf{U}),\tag{2.7}$$

over a suitable space for displacements [52,53]. Existence of a solution of the minimisation problem using pure Dirichlet boundary conditions has been proved in [54,55], and we recall here its application to (2.4).

Theorem 2.1. *Let the stored energy function $\Psi:\mathbb{M}^3_+\to\mathbb{R}$ be continuous and polyconvex with $\Psi(\mathbf{F})=G(\mathbf{F},\operatorname{adj}\mathbf{F})$ on $\mathbb{M}^3_+$, with G coercive. Let $\boldsymbol{b}\in\mathbf{L}^{\frac{p}{p-1}}(\Omega)$ and suppose that the set*

$$\Sigma=\{\boldsymbol{v}\in\mathbf{W}^{1,p}(\Omega):\operatorname{adj}(\nabla\boldsymbol{v})\in\mathbb{L}^q(\Omega,M^3_+),\ \det(\nabla\boldsymbol{v})=1\ \text{a.e. in }\Omega,\quad \boldsymbol{v}=\boldsymbol{g}\ \text{on }\partial\Omega\},$$

is not empty. Assume further that the total stored energy function $S:\Sigma\to\mathbb{R}$ defined by

$$S(\boldsymbol{v})=\int_\Omega\Psi(\nabla\boldsymbol{v})-M(\boldsymbol{v}),$$

satisfies

$$\inf_{\boldsymbol{v}\in\Sigma}S(\boldsymbol{v})<\infty.$$

Then the problem of finding $\mathbf{U}$ *such that*

$$\mathbf{U} \in \Sigma \quad \textit{and} \quad S(\mathbf{U}) = \inf_{\boldsymbol{v}\in\Sigma} S(\boldsymbol{v}),$$

has at least one solution.

Using the three unknowns from our formulation we can recast the standard minimisation problem as a constrained minimisation of (2.7) subject to the constraints

$$\boldsymbol{\Pi} = \frac{\partial \Psi(\mathbf{I}+\nabla\mathbf{U})}{\partial(\mathbf{I}+\nabla\mathbf{U})}(\mathbf{I}+\nabla\mathbf{U})^{\mathtt{t}} - P\mathbf{I}, \tag{2.8a}$$

$$\det(\mathbf{I}+\nabla\mathbf{U}) = 1. \tag{2.8b}$$

An augmented Lagrangian formulation is obtained by including a constraint in the minimisation formulation and writing the constraints in weak form. This will subsequently be useful for controlling the Schur complement of the linearised systems. We therefore minimise the potential energy functional

$$\frac{1}{2}\int_\Omega \Psi(\mathbf{I}+\nabla\mathbf{U}) + \gamma \|\det(\mathbf{I}+\nabla\mathbf{U}) - 1\|^2_{0,\Omega} - M(\mathbf{U}),$$

(where $\gamma \geq 0$ is the augmentation parameter that also influences the convergence of nonlinear solvers), subject to the constraints defined by Eqs. (2.6a) and (2.6c).

Therefore the constrained minimisation results in the Euler–Lagrange equations, which after re-using (2.8a) and splitting the volumetric and shear stress contributions, yields the augmented system

$$\int_\Omega \left[\boldsymbol{\Pi} - \frac{\partial \Psi}{\partial \nabla\mathbf{U}}(\mathbf{I}+\nabla\mathbf{U})^{\mathtt{t}} + P\mathbf{I}\right] : \boldsymbol{\tau} = 0 \qquad \forall \boldsymbol{\tau} \in \mathbb{L}^4_{\mathrm{sym}}(\Omega), \tag{2.9a}$$

$$\int_\Omega \boldsymbol{\Pi}(\mathbf{I}+\nabla\mathbf{U})^{-\mathtt{t}} : \nabla\boldsymbol{v} + \gamma\int_\Omega [\det(\mathbf{I}+\nabla\mathbf{U}) - 1][\det(\mathbf{I}+\nabla\boldsymbol{v}) - 1] = M(\boldsymbol{v}) \qquad \forall \boldsymbol{v} \in \mathbf{H}^1_D(\Omega), \tag{2.9b}$$

$$\int_\Omega [\det(\mathbf{I}+\nabla\mathbf{U}) - 1]\, q = 0 \qquad \forall q \in \mathrm{L}^4(\Omega). \tag{2.9c}$$

Note that the first term in (2.9b) is the same as the left-hand side of (2.6b), which arises from the weak formulation of (2.4b). If $\gamma = 0$, the Euler–Lagrange equation of the minimisation of the potential energy functional also yields this term on the left.

3. Consistent linearisation and solvability

Apart from the discussion in Section 2.4, we do not address in detail the solvability of (2.4), but rather refer to the literature complementing the general theory for well-posedness of hyperelasticity found in e.g. [47,56]. Nevertheless, we briefly address some properties of the Fréchet derivative of the solution operator to the original problem, at a smooth regular exact solution.

3.1. Definition

Consider the following set of coupled PDEs written in mixed form, and arising from a Newton–Raphson linearisation of the equations of hyperelasticity in weak form (2.6): Starting from a sufficiently regular initial guess $(\boldsymbol{\Pi}^{k=0}, \mathbf{U}^{k=0}, P^{k=0})$, for $k = 0, 1, \ldots$, find stress, displacement and pressure increments $(\boldsymbol{\pi}^{k+1}, \boldsymbol{u}^{k+1}, p^{k+1})$ such that

$$\int_\Omega \left[\boldsymbol{\pi}^{k+1} - 2\ \mathrm{sym}\left(\frac{\partial \Psi^k}{\partial \mathbf{F}^k}\cdot[\nabla\boldsymbol{u}^{k+1}]^{\mathtt{t}}\right) + p^{k+1}\mathbf{I}\right] : \boldsymbol{\tau} = \int_\Omega \boldsymbol{\mathcal{R}}^k_{\boldsymbol{\Pi}} : \boldsymbol{\tau} \qquad \forall \boldsymbol{\tau} \in \mathbb{L}^2_{\mathrm{sym}}(\Omega), \tag{3.1a}$$

$$\int_\Omega \left[\boldsymbol{\pi}^{k+1}(\mathbf{F}^k)^{-\mathtt{t}} - \boldsymbol{\Pi}^k(\mathbf{F}^k)^{-\mathtt{t}}[\nabla\boldsymbol{u}^{k+1}]^{\mathtt{t}}(\mathbf{F}^k)^{-\mathtt{t}}\right] : \nabla\boldsymbol{v} = \int_\Omega (\boldsymbol{\mathcal{R}}^k_{\mathrm{U},1} : \nabla\boldsymbol{v} + \boldsymbol{\mathcal{R}}^k_{\mathrm{U},2}\cdot\boldsymbol{v}) + \int_{\partial\Omega_N} \boldsymbol{\mathcal{R}}^k_{\mathrm{U},3}\cdot\boldsymbol{v}$$
$$\forall \boldsymbol{v} \in \mathbf{H}^1_D(\Omega), \tag{3.1b}$$

$$\int_\Omega \left(J^k(\mathbf{F}^k)^{-\mathtt{t}} : \nabla\boldsymbol{u}^{k+1}\right) q = \int_\Omega \mathcal{R}^k_P q \qquad \forall q \in \mathrm{L}^2(\Omega), \tag{3.1c}$$

then update

$$\boldsymbol{\Pi}^{k+1} = \boldsymbol{\Pi}^k + \boldsymbol{\pi}^{k+1}, \quad \mathbf{U}^{k+1} = \mathbf{U}^k + \boldsymbol{u}^{k+1}, \quad P^{k+1} = P^k + p^{k+1},$$

and stop once either the increments or the residuals, in absolute or relative norms, drop below a given tolerance. Here

$$\boldsymbol{\mathcal{R}}^k_{\boldsymbol{\Pi}} = \boldsymbol{\Pi}^k - \frac{\partial \Psi^k}{\partial \mathbf{F}^k}(\mathbf{F}^k)^{\mathtt{t}} + P^k\mathbf{I}, \ \boldsymbol{\mathcal{R}}^k_{\mathbf{U},1} = \boldsymbol{\Pi}^k(\mathbf{F}^k)^{-\mathtt{t}}, \ \boldsymbol{\mathcal{R}}^k_{\mathbf{U},2} = -\rho_0\boldsymbol{b}, \ \boldsymbol{\mathcal{R}}^k_{\mathbf{U},3} = -\boldsymbol{t}, \ \mathcal{R}^k_P = \det(\mathbf{F}^k) - 1,$$

are tensor, vector, and scalar residuals associated with the Newton–Raphson linearisation at the previous step k (including the body load term), and we have used the auxiliary notation $\mathbf{F}^k = \mathbf{I} + \nabla\mathbf{U}^k$, $J^k = \det\mathbf{F}^k$ and $\mathrm{sym}(\boldsymbol{\tau}) = (\boldsymbol{\tau} + \boldsymbol{\tau}^{\mathtt{t}})/2$ for a given tensor $\boldsymbol{\tau}$. As usual, these terms are supposed to be regular enough. In (3.1b)–(3.1c) we have also used the following relations that arise from taking the Gâteaux derivatives of the solution operator in the direction of the displacement increments $\boldsymbol{u}$

$$\frac{\mathrm{d}}{\mathrm{d}\nabla\mathbf{U}}(\mathbf{I} + \nabla\mathbf{U})^{-\mathtt{t}}\big|_{\boldsymbol{u}} = -(\mathbf{F}^k)^{-\mathtt{t}}[\nabla\boldsymbol{u}]^{\mathtt{t}}(\mathbf{F}^k)^{-\mathtt{t}},$$
$$\frac{\mathrm{d}}{\mathrm{d}\nabla\mathbf{U}}\det(\mathbf{I} + \nabla\mathbf{U})\big|_{\boldsymbol{u}} = J^k\left((\mathbf{F}^k)^{-\mathtt{t}} : \nabla\boldsymbol{u}\right)\mathbf{I}.$$

The boundary conditions associated with the linearisation of the strong form (2.4) translate into zero incremental displacement on $\partial\Omega_D$ and zero linearised normal stress on $\partial\Omega_N$. Note also that in (3.1a)–(3.1c) the incremental solutions should now possess the following regularity

$$(\boldsymbol{\pi}^{k+1}, \boldsymbol{u}^{k+1}, p^{k+1}) \in \mathbb{L}^2_{\mathrm{sym}}(\Omega) \times \mathbf{H}^1_D(\Omega) \times \mathrm{L}^2(\Omega).$$

Using the strong form of (3.1a) and the symmetry of $\boldsymbol{\tau}$ we can write

$$\nabla\boldsymbol{u}^{k+1} = \left[2\frac{\partial \Psi^k}{\partial \mathbf{F}^k}\right]^{-1}(\boldsymbol{\pi}^{k+1} + p^{k+1}\mathbf{I} - \boldsymbol{\mathcal{R}}^k_{\boldsymbol{\Pi}}), \tag{3.2}$$

which implies that it is possible to rewrite (3.1c) as follows

$$\int_\Omega \left(J^k(\mathbf{F}^k)^{-\mathtt{t}} : \left[2\frac{\partial \Psi^k}{\partial \mathbf{F}^k}\right]^{-1}(\boldsymbol{\pi}^{k+1} + p^{k+1}\mathbf{I})\right)q = \int_\Omega \mathcal{R}^k_P q + \int_\Omega \left(J^k(\mathbf{F}^k)^{-\mathtt{t}} : \left[2\frac{\partial \Psi^k}{\partial \mathbf{F}^k}\right]^{-1}\boldsymbol{\mathcal{R}}^k_{\boldsymbol{\Pi}}\right)q, \tag{3.3}$$

for all $q \in \mathrm{L}^2(\Omega)$.

As in [3,6] one can suppose that after each Newton step the quantities from the previous iteration and the overall residuals have enough regularity so that the integrals in (3.3) are well-defined.

We cannot continue much further without specifying the form of the strain energy density. In order to make ideas more precise we will focus in the rest of the section on the case of neo-Hookean materials defined by Ψ_{NH} (cf. (2.1)). Then, for the term in (2.6a), we have

$$\frac{\partial \Psi_{\mathrm{NH}}}{\partial \nabla\mathbf{U}} = \mu(\mathbf{I} + \nabla\mathbf{U}).$$

Moreover, the linearisation procedure was done starting from a generic initial guess of the Newton iterates. In case one commences with the stress-free and motionless initial guess, that is,

$$(\boldsymbol{\Pi}^{k=0}, \mathbf{U}^{k=0}, P^{k=0}) = (\mathbf{0}, \mathbf{0}, 0), \tag{3.4}$$

we can simplify further by characterising the following bilinear forms and linear functionals

$$a_1(\boldsymbol{\pi}, \boldsymbol{\tau}) = \frac{1}{2\mu}\int_\Omega \boldsymbol{\pi} : \boldsymbol{\tau}, \quad a_3(p, q) = \frac{d}{2\mu}\int_\Omega pq, \quad b_1(\boldsymbol{u}, \boldsymbol{\tau}) = -\int_\Omega \nabla\boldsymbol{u} : \boldsymbol{\tau}, \quad b_2(p, \boldsymbol{\tau}) = \frac{1}{2\mu}\int_\Omega p\,\mathbf{tr}(\boldsymbol{\tau}),$$
$$F_1(\boldsymbol{\tau}) = \int_\Omega \boldsymbol{\mathcal{R}}_{\boldsymbol{\Pi}} : \boldsymbol{\tau}, \quad F_2(\boldsymbol{v}) = \int_\Omega \boldsymbol{\mathcal{R}}_{\mathbf{U},1} : \nabla\boldsymbol{v} + \int_\Omega \boldsymbol{\mathcal{R}}_{\mathbf{U},2}\cdot\boldsymbol{v} + \int_{\partial\Omega_N} \boldsymbol{\mathcal{R}}_{\mathbf{U},3}\cdot\boldsymbol{v},$$
$$F_3(q) = \int_\Omega \mathcal{R}_P q + \frac{1}{2\mu}\int_\Omega \mathbf{tr}(\boldsymbol{\mathcal{R}}_{\boldsymbol{\Pi}})\,q,$$

in such a way that the first iteration of (3.1) (for a neo-Hookean material) reduces to the symmetric variational problem: Find $(\boldsymbol{\pi}, \boldsymbol{u}, p) \in \mathbb{L}^2_{\mathrm{sym}}(\Omega) \times \mathbf{H}^1_D(\Omega) \times \mathrm{L}^2(\Omega)$ such that

$$\begin{aligned} a_1(\boldsymbol{\pi}, \boldsymbol{\tau}) + b_1(\boldsymbol{u}, \boldsymbol{\tau}) + b_2(p, \boldsymbol{\tau}) &= F_1(\boldsymbol{\tau}) \quad \forall \boldsymbol{\tau} \in \mathbb{L}^2_{\mathrm{sym}}(\Omega), \\ b_1(\boldsymbol{v}, \boldsymbol{\pi}) \qquad\qquad\quad &= F_2(\boldsymbol{v}) \quad \forall \boldsymbol{v} \in \mathbf{H}^1_D(\Omega), \\ b_2(q, \boldsymbol{\pi}) \qquad + a_3(p, q) &= F_3(q) \quad \forall q \in \mathrm{L}^2(\Omega), \end{aligned} \tag{3.5}$$

where we have dropped the iteration index and employed the symmetry of $\boldsymbol{\tau}$. We recall that in displacement–pressure formulations for hyperelasticity one also ends up with symmetric tangent problems (see e.g. [30,56]).

The system (3.5) results from exploiting the linearised counterpart of (3.2), that is

$$\boldsymbol{\pi} - 2\mu\, \mathrm{sym}(\nabla \boldsymbol{u}) + p\mathbf{I} = \mathbf{M},$$

(which implies $\mathbf{tr}(\boldsymbol{\pi}) - 2\mu\, \mathrm{div}\, \boldsymbol{u} + d\, p = \mathbf{trM}$), where $\mathbf{M}$ contains any additional linearisation terms and therefore $(\mathbf{trM})\mathbf{I}$ is absorbed as part of $\boldsymbol{\mathcal{R}}_{\boldsymbol{\Pi}}$ and appears in $F_3(q)$, exactly as in (3.3). Otherwise, in the last equation in (3.5) instead of $b_2(q, \boldsymbol{\pi})$ and $a_3(p, q)$, we should have (as we do have in (3.1c)) a block associated with a bilinear form $b_3(\boldsymbol{u}, q) = \int_\Omega q\, \mathrm{div}\, \boldsymbol{u}$, which would make the problem not block-symmetric:

$$\begin{aligned} a_1(\boldsymbol{\pi}, \boldsymbol{\tau}) + b_1(\boldsymbol{u}, \boldsymbol{\tau}) + b_2(p, \boldsymbol{\tau}) &= F_1(\boldsymbol{\tau}) \quad \forall \boldsymbol{\tau} \in \mathbb{L}^2_{\mathrm{sym}}(\Omega), \\ b_1(\boldsymbol{v}, \boldsymbol{\pi}) \qquad\qquad\quad &= F_2(\boldsymbol{v}) \quad \forall \boldsymbol{v} \in \mathbf{H}^1_D(\Omega), \\ b_3(\boldsymbol{u}, q) \qquad\qquad\quad &= F_3(q) \quad \forall q \in \mathrm{L}^2(\Omega). \end{aligned} \tag{3.6}$$

Note also that system (3.6) corresponds to the weak form of the Navier equations written in terms of the Cauchy stress, the displacement, and the pressure

$$\begin{aligned} \boldsymbol{\pi} - 2\mu\, \mathrm{sym}(\nabla \boldsymbol{u}) + p\mathbf{I} &= \boldsymbol{\mathcal{R}}_{\boldsymbol{\Pi}}, \\ -\mathbf{div}\, \boldsymbol{\pi} &= \boldsymbol{\mathcal{R}}_{\mathbf{U},2}, \\ \mathrm{div}\, \boldsymbol{u} &= \mathcal{R}_P. \end{aligned} \tag{3.7}$$

It is important to remark that if instead of the stress-free initial state (3.4) we take only a motionless state (representing for instance a residual stress present in the system, as typical in soft tissue applications), e.g.

$$(\boldsymbol{\Pi}^{k=0}, \mathbf{U}^{k=0}, P^{k=0}) = (\mathbf{I}, \mathbf{0}, 0),$$

then an additional term appears in (3.7), resulting in the system

$$\begin{aligned} \boldsymbol{\pi} - 2\mu\, \mathrm{sym}(\nabla \boldsymbol{u}) + p\mathbf{I} &= \boldsymbol{\mathcal{R}}_{\boldsymbol{\Pi}}, \\ -\mathbf{div}(\boldsymbol{\pi} - \nabla \boldsymbol{u}^{\mathrm{t}}) &= \boldsymbol{\mathcal{R}}_{\mathbf{U},2}, \\ \mathrm{div}\, \boldsymbol{u} &= \mathcal{R}_P. \end{aligned} \tag{3.8}$$

And similarly as above, after defining the bilinear form

$$a_2(\boldsymbol{u}, \boldsymbol{v}) = \int_\Omega (\nabla \boldsymbol{u})^{\mathrm{t}} : \nabla \boldsymbol{v} = 2 \int_\Omega \mathrm{sym}(\nabla \boldsymbol{u}) : \mathrm{sym}(\nabla \boldsymbol{v}) - \int_\Omega \nabla \boldsymbol{u} : \nabla \boldsymbol{v},$$

the weak forms (3.5) and (3.6) are modified as

$$\begin{aligned} a_1(\boldsymbol{\pi}, \boldsymbol{\tau}) + b_1(\boldsymbol{u}, \boldsymbol{\tau}) + b_2(p, \boldsymbol{\tau}) &= F_1(\boldsymbol{\tau}) \quad \forall \boldsymbol{\tau} \in \mathbb{L}^2_{\mathrm{sym}}(\Omega), \\ b_1(\boldsymbol{v}, \boldsymbol{\pi}) + a_2(\boldsymbol{u}, \boldsymbol{v}) \qquad &= F_2(\boldsymbol{v}) \quad \forall \boldsymbol{v} \in \mathbf{H}^1_D(\Omega), \\ b_2(q, \boldsymbol{\pi}) \qquad + a_3(p, q) &= F_3(q) \quad \forall q \in \mathrm{L}^2(\Omega), \end{aligned} \tag{3.9}$$

and

$$\begin{aligned} a_1(\boldsymbol{\pi},\boldsymbol{\tau}) + b_1(\boldsymbol{u},\boldsymbol{\tau}) + b_2(p,\boldsymbol{\tau}) &= F_1(\boldsymbol{\tau}) \quad \forall \boldsymbol{\tau} \in \mathbb{L}^2_{\mathrm{sym}}(\Omega), \\ b_1(\boldsymbol{v},\boldsymbol{\pi}) + a_2(\boldsymbol{u},\boldsymbol{v}) &= F_2(\boldsymbol{v}) \quad \forall \boldsymbol{v} \in \mathbf{H}^1_D(\Omega), \\ + b_3(\boldsymbol{u},q) &= F_3(q) \quad \forall q \in \mathrm{L}^2(\Omega), \end{aligned} \tag{3.10}$$

respectively.

3.2. Solvability analysis for a linearised and simplified problem

In this section we prove the well-posedness of (3.5). To that end, after simple computations we first observe that (3.5) can be rewritten as:

$$\begin{aligned} \widehat{a}_1(\boldsymbol{\pi},\boldsymbol{\tau}) + b_1(\boldsymbol{u},\boldsymbol{\tau}) + \frac{1}{2\mu}\int_\Omega \left(\frac{1}{d}\mathbf{tr}(\boldsymbol{\pi}) + p\right)\mathbf{tr}(\boldsymbol{\tau}) &= F_1(\boldsymbol{\tau}) \quad \forall \boldsymbol{\tau} \in \mathbb{L}^2_{\mathrm{sym}}(\Omega), \\ b_1(\boldsymbol{v},\boldsymbol{\pi}) &= F_2(\boldsymbol{v}) \quad \forall \boldsymbol{v} \in \mathbf{H}^1_D(\Omega), \\ \frac{1}{2\mu}\int_\Omega \left(\frac{1}{d}\mathbf{tr}(\boldsymbol{\pi}) + p\right) q &= \frac{1}{d}F_3(q) \quad \forall q \in \mathrm{L}^2(\Omega), \end{aligned}$$

with

$$\widehat{a}_1(\boldsymbol{\pi},\boldsymbol{\tau}) = \frac{1}{2\mu}\int_\Omega \boldsymbol{\pi}^{\mathtt{d}} : \boldsymbol{\tau}^{\mathtt{d}},$$

where, for a given tensor field $\boldsymbol{\tau}$, $\boldsymbol{\tau}^{\mathtt{d}}$ is its deviatoric part, that is, $\boldsymbol{\tau}^{\mathtt{d}} = \boldsymbol{\tau} - \frac{1}{d}\mathbf{tr}(\boldsymbol{\tau})\mathbf{I}$. For a given $c \in \mathbb{R}$, $(\boldsymbol{\pi},\boldsymbol{u},p) = (c\mathbf{I},\mathbf{0},-c)$ is a solution to the homogeneous version of (3.5), and as a result the system does not have a unique solution. To fix this from now on we seek the unknown $\boldsymbol{\pi}$ in $\mathbb{L}^2_{0,\mathrm{sym}}(\Omega)$, defined by

$$\mathbb{L}^2_{0,\mathrm{sym}}(\Omega) := \left\{\boldsymbol{\tau} \in \mathbb{L}^2_{\mathrm{sym}}(\Omega) \,:\, \int_\Omega \mathbf{tr}(\boldsymbol{\tau}) = 0\right\},$$

which satisfies $\mathbb{L}^2_{\mathrm{sym}}(\Omega) = \mathbb{L}^2_{0,\mathrm{sym}}(\Omega) \oplus \mathbb{R}\mathbf{I}$. Then, since $\mathbf{tr}(\mathbb{L}^2_{0,\mathrm{sym}}(\Omega)) = \mathrm{L}^2_0(\Omega)$, with

$$\mathrm{L}^2_0(\Omega) := \left\{q \in \mathrm{L}^2(\Omega) \,:\, \int_\Omega q = 0\right\},$$

satisfying $\mathrm{L}^2(\Omega) = \mathrm{L}^2_0(\Omega) \oplus \mathbb{R}$, we readily obtain that, after restricting the trial and test spaces associated with the unknown $\boldsymbol{\pi}$ to $\mathbb{L}^2_{0,\mathrm{sym}}(\Omega)$, (3.5) is equivalent to the problem: Find $(\boldsymbol{\pi},\boldsymbol{u}) \in \mathbb{L}^2_{0,\mathrm{sym}}(\Omega) \times \mathbf{H}^1_D(\Omega)$ such that

$$\begin{aligned} \widehat{a}_1(\boldsymbol{\pi},\boldsymbol{\tau}) + b_1(\boldsymbol{u},\boldsymbol{\tau}) &= F_1(\boldsymbol{\tau}) - \frac{1}{d}F_3(\mathbf{tr}(\boldsymbol{\tau})) \quad \forall \boldsymbol{\tau} \in \mathbb{L}^2_{0,\mathrm{sym}}(\Omega), \\ b_1(\boldsymbol{v},\boldsymbol{\pi}) &= F_2(\boldsymbol{v}) \quad \forall \boldsymbol{v} \in \mathbf{H}^1_D(\Omega). \end{aligned} \tag{3.11}$$

We prove that (3.11) is well-posed to prove the well-posedness of (3.5). To do that, we establish the following technical result.

Lemma 3.1. *There exists $C > 0$ such that*

$$\|\boldsymbol{\tau}^{\mathtt{d}}\|_{0,\Omega} \geq C\|\boldsymbol{\tau}\|_{0,\Omega}, \quad \forall \boldsymbol{\tau} \in \mathrm{Ker}\,(b_1) := \{\boldsymbol{\tau} \in \mathbb{L}^2_{0,\mathrm{sym}}(\Omega) : \int_\Omega \nabla \boldsymbol{v} : \boldsymbol{\tau} = 0 \quad \forall\, \boldsymbol{v} \in \mathbf{H}^1_D(\Omega)\}.$$

Proof. We proceed similarly to the proof of [57, Lemma 2.3]. In fact, we let $\boldsymbol{\tau} \in \mathrm{Ker}(b_1)$ and observe that since $\int_\Omega \mathbf{tr}(\boldsymbol{\tau}) = 0$, there exists $\boldsymbol{z} \in \mathbf{H}^1_D(\Omega)$ such that (see [58, Corollary 2.4])

$$\mathrm{div}\,\boldsymbol{z} = -\mathbf{tr}(\boldsymbol{\tau}) \quad \text{in} \quad \Omega \quad \text{and} \quad \|\boldsymbol{z}\|_{1,\Omega} \leq C\|\mathbf{tr}(\boldsymbol{\tau})\|_{0,\Omega}.$$

It follows that

$$\|\mathbf{tr}(\boldsymbol{\tau})\|^2_{0,\Omega} = \int_\Omega \mathbf{tr}(\boldsymbol{\tau})\,\mathrm{div}\,\boldsymbol{z} = \int_\Omega \nabla \boldsymbol{z} : (\mathbf{tr}(\boldsymbol{\tau})\mathbf{I}).$$

Then, since $\mathbf{tr}(\boldsymbol{\tau})\mathbf{I} = d(\boldsymbol{\tau} - \boldsymbol{\tau}^{\mathrm{d}})$ and $\int_\Omega \nabla z : \boldsymbol{\tau} = 0$, it readily follows that

$$\|\mathbf{tr}(\boldsymbol{\tau})\|^2_{0,\Omega} = \int_\Omega \nabla z : \boldsymbol{\tau}^{\mathrm{d}} \leq \|z\|_{1,\Omega}\|\boldsymbol{\tau}^{\mathrm{d}}\|_{0,\Omega} \leq C\|\mathbf{tr}(\boldsymbol{\tau})\|_{0,\Omega}\|\boldsymbol{\tau}^{\mathrm{d}}\|_{0,\Omega},$$

which together with the fact that $\|z\|_{1,\Omega} \leq C\|\mathbf{tr}(\boldsymbol{\tau})\|_{0,\Omega}$, implies

$$\|\mathbf{tr}(\boldsymbol{\tau})\|_{0,\Omega} \leq C\|\boldsymbol{\tau}^{\mathrm{d}}\|_{0,\Omega}.$$

This estimate, and the identity $\|\boldsymbol{\tau}\|^2_{0,\Omega} = \|\boldsymbol{\tau}^{\mathrm{d}}\|^2_{0,\Omega} + \frac{1}{d}\|\mathbf{tr}(\boldsymbol{\tau})\|^2_{0,\Omega}$, imply the result. □

Now we are in position of proving the well-posedness of (3.5).

Theorem 3.1. *There exists a unique solution* $(\boldsymbol{\pi}, \boldsymbol{u}, p) \in \mathbb{L}^2_{0,\mathrm{sym}}(\Omega) \times \mathbf{H}^1_D(\Omega) \times \mathrm{L}^2(\Omega)$ *to* (3.5).

Proof. According to the above, in what follows we prove equivalently that problem (3.11) is well-posed by means of the Babuška–Brezzi theory.

We begin by noticing that the ellipticity of $\widehat{a}_1(\boldsymbol{\pi}, \boldsymbol{\tau})$ on $\mathrm{Ker}(b_1)$ is a direct consequence of Lemma 3.1. Now, given $\boldsymbol{v} \in \mathbf{H}^1_D(\Omega)$, we let $\tilde{\boldsymbol{\tau}} = -\mathrm{sym}(\nabla \boldsymbol{v})$ and observe that

$$\int_\Omega \mathbf{tr}(\tilde{\boldsymbol{\tau}}) = -\int_\Omega \mathrm{div}\, \boldsymbol{v} = -\int_{\partial\Omega} \boldsymbol{v}\cdot\boldsymbol{n} = 0,$$

which implies that $\tilde{\boldsymbol{\tau}} \in \mathbb{L}^2_{0,\mathrm{sym}}(\Omega)$. In addition, the well-known Korn and Poincaré inequalities (see, e.g., [59, Corollaries 9.2.22, 9.2.25 and Proposition 5.3.5]) imply that

$$\|\tilde{\boldsymbol{\tau}}\|_{0,\Omega} = \|\mathrm{sym}(\nabla \boldsymbol{v})\|_{0,\Omega} \geq C\|\boldsymbol{v}\|_{1,\Omega}. \tag{3.12}$$

Then observing that $\tilde{\boldsymbol{\tau}} : \nabla \boldsymbol{v} = -\tilde{\boldsymbol{\tau}} : \tilde{\boldsymbol{\tau}}$, it follows that

$$\sup_{\substack{\boldsymbol{\tau}\in\mathbb{L}^2_{0,\mathrm{sym}}(\Omega)\\ \boldsymbol{\tau}\neq\mathbf{0}}} \frac{b_1(\boldsymbol{v},\boldsymbol{\tau})}{\|\boldsymbol{\tau}\|_{0,\Omega}} \geq \frac{b_1(\boldsymbol{v},\tilde{\boldsymbol{\tau}})}{\|\tilde{\boldsymbol{\tau}}\|_{0,\Omega}} = \|\tilde{\boldsymbol{\tau}}\|_{0,\Omega},$$

which, in combination with (3.12), implies that b_1 satisfies the required inf–sup condition, thus finishing the proof. □

We end this section by observing that if we employ the same techniques used to establish well-posedness of (3.9) to study (3.10), then the results hold under a restriction on the bulk modulus.

4. Mixed finite element scheme and preconditioner

4.1. A Galerkin method

Let us denote by $\mathcal{T}_h$ a regular partition of Ω into simplices (triangles or tetrahedra) K of maximum diameter h_K, and define the mesh size as $h := \max\{h_K : K \in \mathcal{T}_h\}$. The set of facets (the skeleton of the mesh) will be denoted $\mathcal{E}_h$. In the lowest-order case, the specific finite element method we choose here is based on solving the discrete weak form of the hyperelasticity equations using piecewise constant approximations of the symmetric Kirchhoff stress tensor, piecewise linear approximation of displacements, and piecewise constant approximation of solid pressure. More generally, for $\ell \in \mathbb{N} \cup \{0\}$ we use the finite dimensional spaces $\mathbb{H}_h \subset \mathbb{L}^2_{\mathrm{sym}}(\Omega)$, $\mathbf{V}_h \subset \mathbf{H}^1(\Omega)$, $Q_h \subset \mathrm{L}^2(\Omega)$ defined as follows:

$$\begin{aligned}
&\mathbb{H}_h := \{\boldsymbol{\tau}_h \in \mathbb{L}^2_{\mathrm{sym}}(\Omega) : \boldsymbol{\tau}_h|_K \in \mathbb{P}_\ell(K)^{d\times d}\ \forall K \in \mathcal{T}_h\},\\
&\mathbf{V}_h := \{\boldsymbol{v}_h \in \mathbf{H}^1(\Omega) : \boldsymbol{v}_h|_K \in \mathbb{P}_{\ell+1}(K)^d\ \forall K \in \mathcal{T}_h,\ \ \boldsymbol{v}_h|_{\partial\Omega_D} = \mathbf{0}\},\\
&Q_h := \{q_h \in \mathrm{L}^2(\Omega) : q_h|_K \in \mathbb{P}_\ell(K)\ \forall K \in \mathcal{T}_h\},
\end{aligned} \tag{4.1}$$

where $\mathbb{P}_r(R)$ denotes the space of polynomial functions of degree $s \leq r$ defined on the set R.

The Galerkin scheme associated with (3.9) is then defined as

$$\begin{aligned} a_1(\boldsymbol{\pi}_h, \boldsymbol{\tau}_h) + b_1(\boldsymbol{u}_h, \boldsymbol{\tau}_h) &+ b_2(p_h, \boldsymbol{\tau}_h) = F_1(\boldsymbol{\tau}_h) && \forall \boldsymbol{\tau}_h \in \mathbb{H}_h, \\ b_1(\boldsymbol{v}_h, \boldsymbol{\pi}_h) + a_2(\boldsymbol{u}_h, \boldsymbol{v}_h) &= F_2(\boldsymbol{v}_h) && \forall \boldsymbol{v}_h \in \mathbf{V}_h, \\ b_2(q_h, \boldsymbol{\pi}_h) &+ a_3(p_h, q_h) + \beta \sum_{e \in \mathcal{E}_h} \int_e h_e [\![p_h]\!][\![q_h]\!] = F_3(q_h) && \forall q_h \in Q_h, \end{aligned} \tag{4.2}$$

where the discrete spaces are defined as in (4.1) and where β is a positive, pressure stabilisation parameter independent of the mesh size, required in this simplicial counterpart of the finite element method for quadrilaterals studied in [22]. The symbol $[\![q]\!]$ denotes the jump of the generic scalar field q over a given facet $e \in \mathcal{E}_h$.

4.2. An augmented Lagrangian preconditioner

Augmented Lagrangian preconditioners can be applied either on the continuous level (modifying the variational formulation) or the discrete level (manipulating matrices after assembly). These strategies sometimes coincide, but are in general distinct. In this work we employ the continuous strategy, solving (2.9). However, to build intuition for how adding an augmented Lagrangian helps control the Schur complement, it is easier to begin with an explanation of the discrete formulation.

The discrete form of the general tangent problem (3.1) can be written as

$$\mathcal{M} \begin{pmatrix} \boldsymbol{\pi}_h \\ \boldsymbol{u}_h \\ p_h \end{pmatrix} = \begin{bmatrix} \mathcal{A}_1 & \mathcal{B}_1 & \mathcal{B}_2 \\ \tilde{\mathcal{B}}_1 & \mathcal{A}_2 & O \\ \tilde{\mathcal{B}}_2 & O & \mathcal{A}_3 \end{bmatrix} \begin{pmatrix} \boldsymbol{\pi}_h \\ \boldsymbol{u}_h \\ p_h \end{pmatrix} = \begin{pmatrix} \mathcal{F}_1 \\ \mathcal{F}_2 \\ \mathcal{F}_3 \end{pmatrix}. \tag{4.3}$$

In order to fit (4.3) into the preconditioning framework described previously in Section 1, it is desirable to rearrange $\mathcal{M}$ as a 2×2 block matrix. We therefore treat $(\boldsymbol{\pi}_h, \boldsymbol{u}_h)$ together as one field and p_h as another.

The linear system after splitting becomes

$$\mathcal{A} \begin{pmatrix} \mathcal{U}_h \\ p_h \end{pmatrix} = \begin{pmatrix} \boldsymbol{\kappa} \\ \tilde{b} \end{pmatrix}, \tag{4.4}$$

where

$$\begin{bmatrix} A & B \\ C & D \end{bmatrix} := \mathcal{A},$$

with A being a 2×2 block matrix, B being a 2×1 block matrix, C being a 1×2 block, $D = \mathcal{A}_3$, and

$$\mathcal{U}_h = \begin{pmatrix} \boldsymbol{\pi}_h \\ \boldsymbol{u}_h \end{pmatrix}, \quad \boldsymbol{\kappa} = \begin{pmatrix} \mathcal{F}_1 \\ \mathcal{F}_2 \end{pmatrix}, \quad \tilde{b} = \mathcal{F}_3.$$

We recall that the constraint imposed on the mechanical problem is $J - 1 = 0$, so the augmentation added to the weak form of the variational formulation is the Fréchet derivative of the term

$$\frac{\gamma}{2} \int_\Omega (J-1)^2.$$

The larger the value we take for γ, the more we penalise violation of the constraint. In fact, if γ is taken large enough, it provides an alternative to the use of the Lagrange multiplier p for enforcing the constraint, although the augmented Lagrangian approach is preferable to this pure penalty formulation. Following from the similar ideas in [60], the linear system (4.4) after discrete augmentation then becomes

$$\mathcal{A}_\gamma \begin{pmatrix} \mathcal{U}_h \\ p_h \end{pmatrix} = \begin{bmatrix} A_\gamma & B \\ C & D \end{bmatrix} \begin{pmatrix} \mathcal{U}_h \\ p_h \end{pmatrix} = \begin{pmatrix} \boldsymbol{\kappa} \\ \tilde{b} \end{pmatrix},$$

where

$$A_\gamma = A + \gamma B M_p^{-1} C,$$

and M_p is the pressure mass matrix. We construct the preconditioner based on the block factorisation formula

$$\mathcal{P}^{-1} = \begin{bmatrix} I & -\hat{A}_\gamma^{-1} B \\ 0 & I \end{bmatrix} \begin{bmatrix} \hat{A}_\gamma^{-1} & 0 \\ 0 & \hat{S}_\gamma^{-1} \end{bmatrix} \begin{bmatrix} I & 0 \\ -C\hat{A}_\gamma^{-1} & I \end{bmatrix}. \tag{4.5}$$

The smaller sparse linear system associated with the top-left block $\hat{A}_\gamma$ (i.e. the approximation of A_γ) is solved directly by the standard LU factorisation. The dense Schur complement approximation $\hat{S}_\gamma$ in (4.5), on the other hand, requires more consideration. Following from the definition of the Schur complement, S_γ can be expressed as

$$S_\gamma = D - CA_\gamma^{-1}B = D - C(A + \gamma B M_p^{-1}\ C)^{-1}B,$$

and can be simplified by the Sherman–Morrison–Woodbury inverse formula [61]:

$$S_\gamma = D + (-(CA^{-1}B)^{-1} - \gamma M_p^{-1})^{-1}. \tag{4.6}$$

By increasing the value of γ we are able to capture the dominating term in (4.6). An adequate approximation $\hat{S}_\gamma$ is thus obtained simply by neglecting the dominated terms. The resulting Schur complement approximation is then given by

$$\hat{S_\gamma} = D + (-\gamma M_p^{-1})^{-1} = -\frac{1}{\gamma}M_p + D.$$

In the simplified setting of (3.9) (and of (3.10)), and exploiting the fact that the same discrete space is used for the pressure and for the components of the stress, the augmentation consists of adding a term

$$\frac{\gamma}{4\mu^2}\int_\Omega \mathbf{tr}(\boldsymbol{\pi})\mathbf{tr}(\boldsymbol{\tau}),$$

to the stress–stress block. Strikingly, the continuous augmentation instead adds a term to the displacement-displacement block. This structural distinction does not occur in other problems, such as in stress–velocity–pressure formulations for non-Newtonian flow [62]; here it is caused by the fact that the pressure appears in the equation for the stress (2.9a), rather than the equation for the displacement (2.9b). Nevertheless, the continuous augmentation also successfully controls the Schur complement of the linearised systems [63, Lemma 3].

The processes of solving the separate linear systems associated with $\hat{A}_\gamma$ and $\hat{S}_\gamma$ (with either the continuous or discrete augmentation) are known as the inner solves, and the process of solving the overall coupled system after preconditioning is called the outer solve. We adopt a single GMRES iteration preconditioned by direct factorisations of $\hat{A}_\gamma$ and $\hat{S}_\gamma$ for the inner solves, and use standard FGMRES iteration for the outer solve [64]. Multigrid algorithms for the augmented block are complicated by the addition of a term with a large kernel. The iterative solution of the augmented block, following the general principles of multigrid for nearly singular problems [65], will be investigated in future work.

5. Numerical examples

In this section we present a set of computational tests that serve as verification of the convergence of the mixed method in the linear and nonlinear cases. We also explore the applicability of the formulation in computing some benchmark solutions [8]. All routines have been implemented using the open source finite element libraries FEniCS [66] and Firedrake [67].

5.1. Accuracy verification

On the domain $\Omega = (0,1)^2$ we consider the following closed-form displacement and pressure solving the nonlinear problem (2.4)

$$\mathbf{U} = 0.1(y^2, y^3)^{\mathrm{t}}, \quad P = x^4 - y^4,$$

and $\boldsymbol{\Pi}$ is computed with these solutions using (2.3). We consider both neo-Hookean and Holzapfel–Ogden materials and prescribe the interpolant of the exact displacement on the whole boundary. The mean value of pressure is fixed through a real Lagrange multiplier. These solutions satisfy the incompressibility constraint, and the body load is manufactured from the exact solutions and (2.4b). The material parameter for the neo-Hookean energy is $\mu = 100$, whereas the model parameters for the Holzapfel–Ogden energy are (see, e.g., [68–71])

$$a = 0.496, \quad b = 0.041, \quad a_f = 0.193, \quad b_f = 0.176, \quad a_s = 0.123, \quad b_s = 0.209,$$
$$a_{fs} = 0.162, \quad b_{fs} = 0.166, \quad \boldsymbol{f}_0 = (1,0)^{\mathrm{t}}, \quad \boldsymbol{s}_0 = (0,-1)^{\mathrm{t}}.$$

Table 5.1
Test 1: Error history for Kirchhoff stress, displacement, and pressure; associated with the mixed finite element method using different polynomial degrees $\ell \in \{0, 1\}$ and for neo-Hookean and Holzapfel–Ogden material laws.

DoF	h	$\lvert\boldsymbol{\Pi} - \boldsymbol{\Pi}_h\rvert_{0,\Omega}$	rate	$\lvert\mathbf{U} - \mathbf{U}_h\rvert_{1,\Omega}$	rate	$\lvert P - P_h\rvert_{0,\Omega}$	rate
neo-Hookean with $\ell = 0$							
51	0.707	65.20	–	0.057	–	32.22	–
179	0.353	27.81	1.229	0.029	0.997	12.31	1.388
675	0.176	12.61	1.143	0.014	1.002	5.222	1.237
2,627	0.088	6.004	1.069	0.007	1.002	2.412	1.114
10,371	0.044	2.938	1.031	0.003	1.001	1.165	1.050
41,219	0.022	1.455	1.014	0.001	1.000	0.573	1.023
neo-Hookean with $\ell = 1$							
147	0.707	3.483	–	0.005	–	1.035	–
547	0.353	0.795	2.130	0.001	2.047	0.143	2.848
2,115	0.176	0.193	2.042	3.5e−4	2.012	0.023	2.624
8,323	0.088	0.047	2.014	8.7e−5	2.003	0.004	2.345
33,027	0.044	0.011	2.005	2.1e−5	2.001	0.001	2.143
131,587	0.022	0.004	2.001	5.1e−6	2.000	2.5e−4	2.056
Holzapfel–Ogden with $\ell = 0$							
51	0.707	0.966	–	0.058	–	0.512	–
179	0.353	0.434	1.154	0.029	0.992	0.213	1.259
675	0.176	0.198	1.133	0.014	1.012	0.093	1.191
2,627	0.088	0.093	1.084	0.007	1.009	0.043	1.115
10,371	0.044	0.045	1.045	0.004	1.005	0.021	1.059
41,219	0.022	0.022	1.022	0.002	1.003	0.010	1.029
Holzapfel–Ogden with $\ell = 1$							
147	0.707	0.164	–	0.006	–	0.088	–
547	0.353	0.041	2.007	0.001	2.001	0.021	2.074
2115	0.176	0.010	1.999	3.7e−4	2.082	0.005	2.021
8323	0.088	0.002	2.001	8.9e−5	2.062	0.001	2.007
33,027	0.044	6.3e−4	2.001	2.2e−5	2.025	3.2e−4	2.004
131,587	0.022	1.6e−4	1.999	5.2e−6	2.001	7.9e−5	2.002

Table 5.2
Test 1: Error history for stress, displacement, and pressure in the linear regime (3.8), with $\beta = 10^{-4}$.

DoFs	h	$\lvert\boldsymbol{\pi} - \boldsymbol{\pi}_h\rvert_{0,\Omega}$	rate	$\lvert\boldsymbol{u} - \boldsymbol{u}_h\rvert_{1,\Omega}$	rate	$\lvert p - p_h\rvert_{0,\Omega}$	rate
Linear, block symmetric (4.2) with $\ell = 0$							
51	0.707	22.87	–	0.051	–	13.86	–
179	0.353	9.849	1.216	0.025	0.996	5.632	1.299
675	0.176	4.503	1.129	0.012	1.000	2.466	1.192
2627	0.088	2.151	1.066	0.006	1.000	1.148	1.103
10,371	0.044	1.052	1.032	0.003	1.000	0.553	1.052
41,219	0.022	0.525	1.016	0.001	1.000	0.272	1.026
164,355	0.011	0.259	1.008	8.0e−4	1.000	0.135	1.013
Linear, block symmetric (4.2) with $\ell = 1$							
147	0.707	4.358	–	0.004	–	2.843	–
547	0.353	0.806	2.433	0.001	2.022	0.499	2.351
2115	0.176	0.178	2.177	2.6e−4	2.013	0.107	2.225
8323	0.088	0.042	2.075	6.5e−5	2.006	0.025	2.099
33,027	0.044	0.010	2.032	1.6e−5	2.003	0.006	2.043
131,587	0.022	0.002	2.015	4.1e−6	2.001	0.001	2.019

The stabilisation parameter in the neo-Hookean test is $\beta = 10^{-4}$ and in the Holzapfel–Ogden case is $\beta = 10^{-2}$. These constants are chosen heuristically.

We implement a Newton–Raphson method that stops whenever a residual absolute tolerance of 10^{-8} is attained, and where at each iteration the discrete version of the linear system (3.1) is solved with the Multifrontal Massively Parallel Sparse direct Solver (MUMPS). We then do uniform mesh refinement and on each level we compute errors between approximate and exact solutions and record the absolute errors and convergence rates in Table 5.1, which indicate optimal error decay for the first- and second-order cases.

We also conduct an experimental convergence test for the linearised Galerkin scheme (4.2). Now the exact solutions satisfying (3.8) are

$$\boldsymbol{u} = 0.1(y^2, y^3)^{\mathrm{t}}, \quad p = x^4 - y^4, \quad \boldsymbol{\pi} = 2\mu\mathrm{sym}(\nabla \boldsymbol{u}) - p\mathbf{I},$$

and the external load is $\boldsymbol{b} = -\frac{1}{\rho_0}\mathbf{div}(\boldsymbol{\pi} - \nabla \boldsymbol{u}^{\mathrm{t}})$. We again take $\mu = 100$ and the error history is displayed in Table 5.2, where we use $\beta = 10^{-4}$. We observe the expected rates of convergence. Unreported numerical experiments indicate that the discretisation of the nonsymmetric formulation arising from (3.10) obtains the same results.

5.2. Inhomogeneous compression benchmark in 2D

We study the deformation of a rectangular block that undergoes a pressure load (here implemented as a traction) applied on the centre of the top edge. The domain is $\Omega = (0, 20) \times (0, 10)$ (in mm^2), the shear modulus is $\mu = 240.565/(2(1 + 0.4999))\,\mathrm{MPa}$ and the applied pressure is $P_0 = 400\,\mathrm{MPa}$. On the top surface we prescribe zero tangential displacement, on the bottom we set zero normal displacement, and on the vertical boundaries we impose zero traction. As in [8], we record the vertical displacement on the centre of the top boundary for different levels of mesh resolution, for different polynomial degrees, and different values of the stabilisation parameter. The results are portrayed in the right plot of Fig. 5.1. We observe how the output converges to the value -5.63, which agrees with the results from [8]. We can also see that for the first and second-order methods, the value $\beta = 0.001$ performs best. In the higher-order case the result is insensitive to the stabilisation, while in the lowest-order case the convergence with e.g. $\beta = 0.1$ is very poor. The number of Newton iterations is not shown as it practically coincides in all cases, and it varies between 5–6 steps. Classical strain enhancing methods may exhibit the so-called hourglass instability for this compression test (see, e.g., [16,72]), and this is not observed in the present set of simulations.

5.3. Compression test in 3D

We consider the example of a hollow cylinder deforming under compression and shear in 3D [6, Sect. 5.3.2]. As in the previous example we employ an isotropic and incompressible neo-Hookean material now with shear modulus $\mu = 50$, and consider a hollow cylinder of height 4 cm, inner radius 0.75 cm and outer radius 1 cm. The domain is discretised into 23,946 tetrahedral elements yielding, for the lowest-order scheme, a total of 180,134 DoFs. The stabilisation is set to $\beta = 0.1$. The surface defined by $z = 0$ is clamped and the surface at $z = 4$ undergoes an increasing deformation. In contrast with Test 2, here we apply an incremental load taking 10 intermediate steps and progressively reaching a maximal displacement on the top surface of magnitude 1.5, and acting only in the directions x and z, equally. On the inner and outer radii we prescribe zero traction. The deformations induced by shear are seen from Fig. 5.2, where we plot Kirchhoff stress components and pressure on the deformed domain, showing the undeformed configuration with opacity. The overall behaviour of the simulation agrees with the results from [6].

5.4. Twist and contraction of left ventricle

Next we conduct a simple test on a patient-specific left ventricular geometry segmented from CT-scans. The basal region (the top surface) corresponds to $\partial\Omega_D$ where normal displacements are set to zero, whereas the epicardium and endocardium constitute $\partial\Omega_N$. On the endocardium we set an incremental traction increasing from $\mathbf{0}$ to $3\boldsymbol{n}$ (where $\boldsymbol{n}$ is the normal vector on the boundary), which represents the variation of endocardial pressure from zero to 3 kPa in a sub-stage of the ejection phase. On the epicardium we simply set zero traction. The directions of fibre and sheetlet orientation are generated with a Laplace–Dirichlet rule-based method in mixed form as described in [24] (its primal counterpart was proposed in [73] and other variants used in, e.g., [74]), and the resulting muscle fibres have an orientation varying transmurally from the epicardial surface to the endocardial surface with

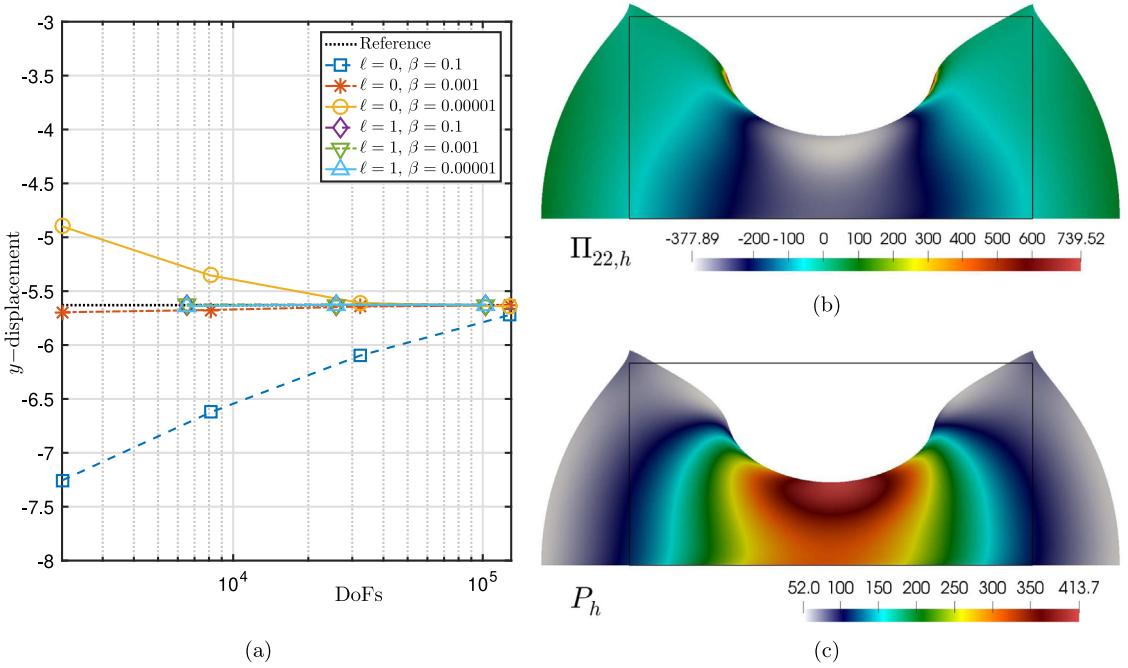

Fig. 5.1. Test 2: inhomogeneous compression of a neo-Hookean block. Left: vertical displacement on the top-centre of the domain according to the number of degrees of freedom and for different values of the pressure stabilisation. Right: yy-component of the Kirchhoff stress and pressure distribution plotted on the deformed configuration, computed with $\ell = 0$ and $\beta = 0.001$. For this case the displacement on the centre of the top edge is $\boldsymbol{u} = (0, -5.71)^{\mathrm{t}}$.

a difference of 120 degrees, whereas the collagen sheetlets have a radial distribution relative to the ventricular centreline. This ventricular centreline is aligned with the z-axis, the apex-to-base distance is 10.13 cm, and the maximal circumferential radius is 3.94 cm. We generate a tetrahedral mesh of 94,269 cells and 22,193 vertices on which we implement the mixed scheme with $\ell = 1$ and $\beta = 50$. We employ the Holzapfel–Ogden material law with the constitutive parameters used in Example 1. The active contraction of the ventricle is incorporated through the so-called active strain approach (see, e.g., [23]) where the activation function ξ is incremented together with the endocardial pressure up to a maximal activation of 12%. In order to achieve sufficient torsion and thickening of the ventricular wall, we also use an algebraic relation between the activation and the myocyte shortening that models sliding myofilaments of collagen and a transmurally heterogeneous activation that modulates different values of ξ in each direction (see details in [75,76])

$$\xi_f = \xi, \quad \xi_n = (1-\zeta)k_0\xi + \zeta[(1-\xi)^{-1/2} - 1], \quad \xi_s = (1+\xi)^{-1}(1+\xi_n)^{-1} - 1,$$

where ζ is a smooth indicator function going from 0 on the endocardium to 1 on the epicardium, and we choose a mild orthotropic activation parameter of $k_0 = 3$.

In Fig. 5.3 we plot two snapshots of the obtained solutions, one at the beginning of the diastolic phase and the second one for the end-diastolic configuration. Stresses and pressure concentrate in the vicinity of the interface between the basal region and the endocardium, and we see the expected apex-to-base contraction together with a deformation following the fibre orientation and producing a more pronounced wall thickening towards the basal epicardium. In some regions the mesh is not visible because the deformed geometry has moved in the positive x-direction.

It is worth remarking that fine-mesh simulations for realistic and patient-specific geometries are not possible using only direct solvers due to the excessive memory usage. This issue intensifies in more complex models such as electromechanical tests. Adopting the augmented Lagrangian strategy, even with direct solvers for the top-left block, enables larger-scale and more complex computations.

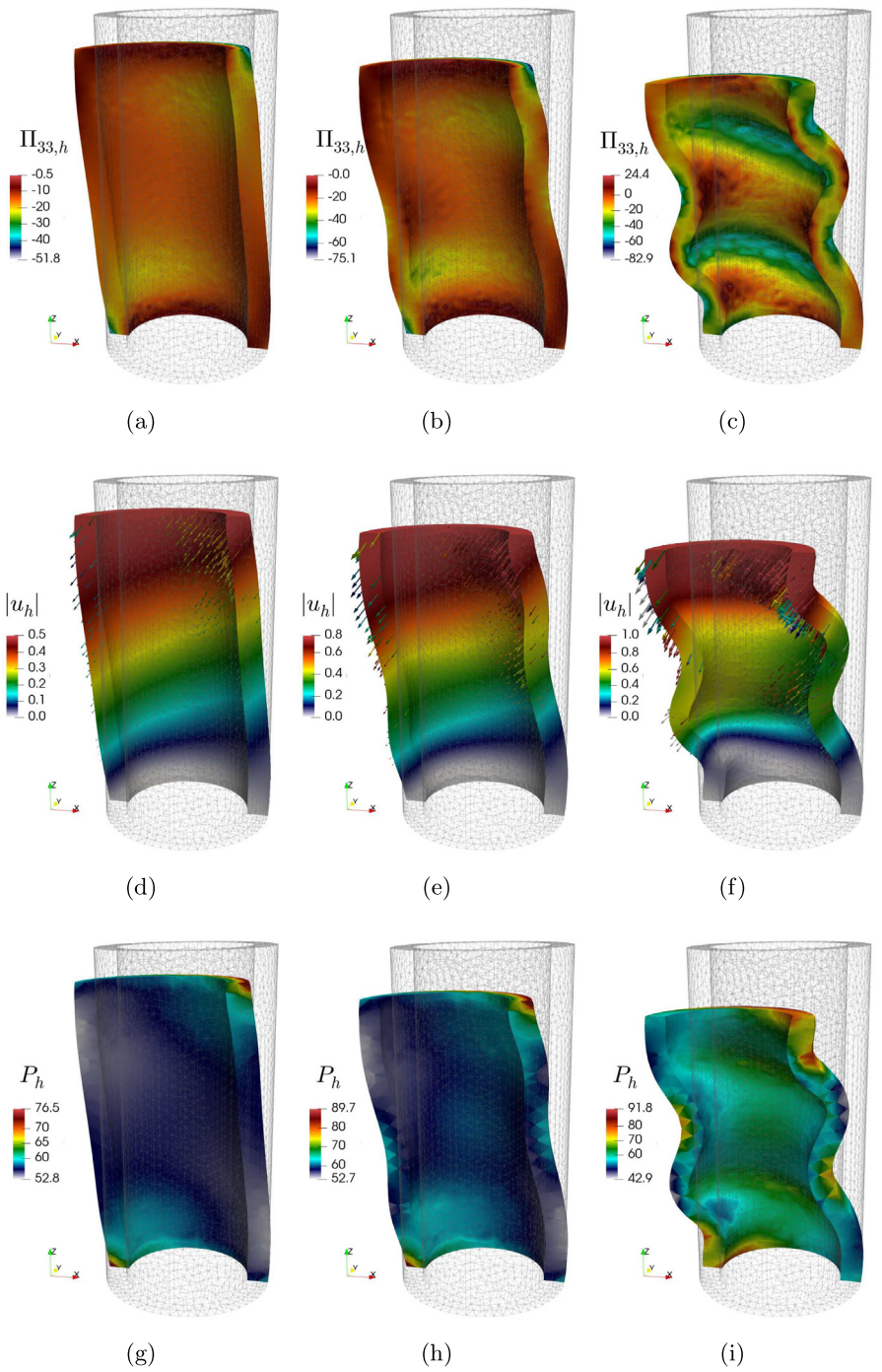

Fig. 5.2. Test 3: compressing a neo-Hookean hollow cylinder for three incremental loadings (from left to right), using $\ell = 0$ and $\beta = 0.1$. Top: zz-component of the Kirchhoff stress. Middle: displacement magnitude and arrows. Bottom: pressure distribution plotted on the deformed configuration.

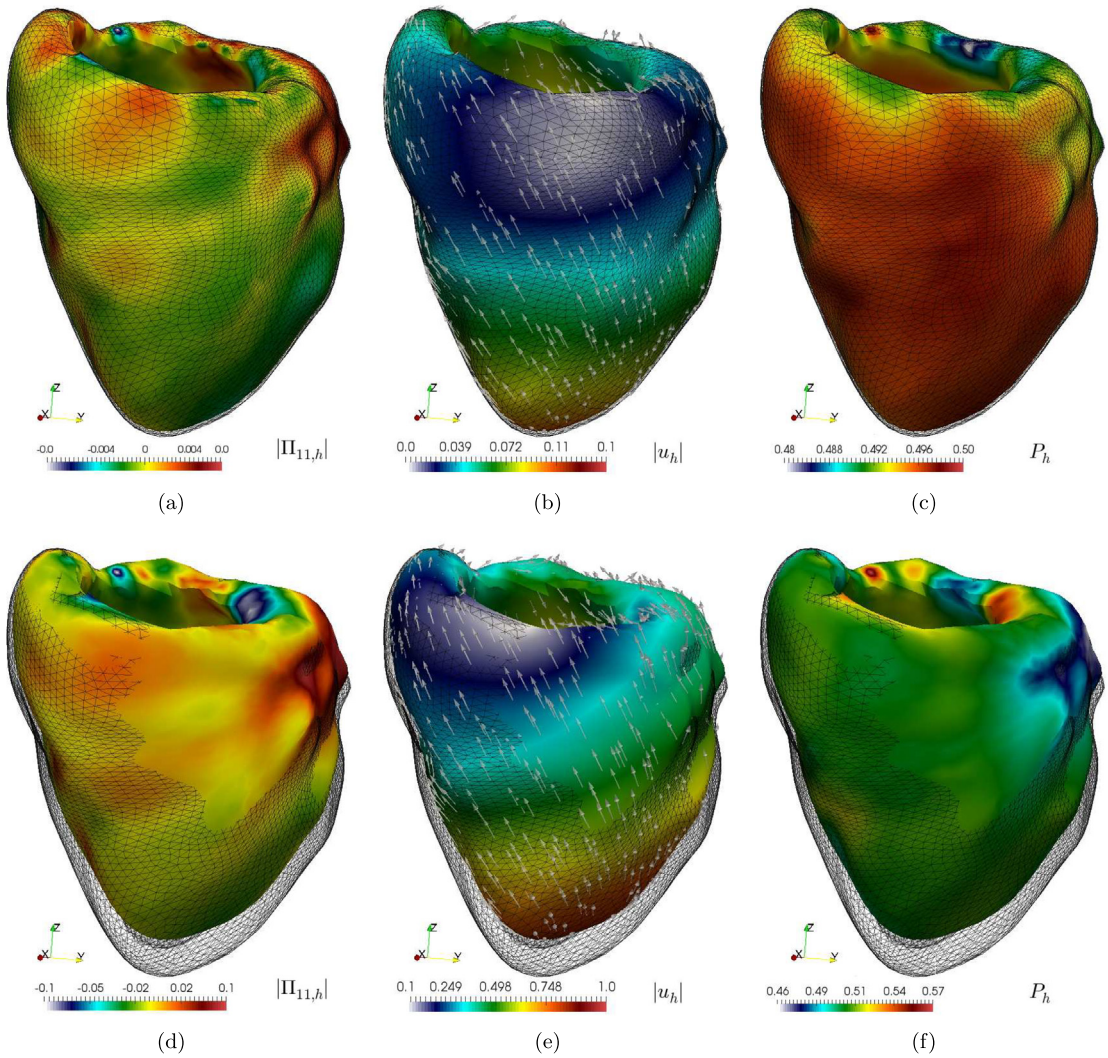

Fig. 5.3. Test 4: contraction of an orthotropic cardiac ventricle for two and seven incremental steps of active strain loading (top and bottom, respectively). The Holzapfel–Ogden material law has been used. Left: xx-component of the Kirchhoff stress. Middle: displacement magnitude and arrows. Right: pressure distribution plotted on the deformed configuration.

5.5. Performance of the preconditioner

We employ a set of computational benchmark problems introduced in [77] for cardiac biomechanics, as examples where we examine the accuracy and the performance of the augmented Lagrangian solvers. These tests have been used in [35] in the context of preconditioning. Detailed descriptions of the problems can be found therein. Here we simulate only the first two tests (namely the beam deflection problem and the ellipsoid inflation problem), since the equivalence of the contraction problem has already been considered in Section 5.4. Quantitative results (i.e. the deflection and inflation magnitudes), which allow us to validate the accuracy of the discretisation and preconditioner are given in the recent work [35], and the performance of the preconditioner can be examined by looking at the average number of outer Krylov iterations per Newton step and total runtime.

The first problem (Test 5) considers a deflecting cuboidal beam whose geometry is defined by $x \in [0, 10]$, $y \in [0, 1]$, $z \in [0, 1]$ mm, with the fibre direction being constant along the x-axis. To match the benchmark test in [77], the transversely isotropic constitutive law is characterised by the strain energy density proposed by Guccione

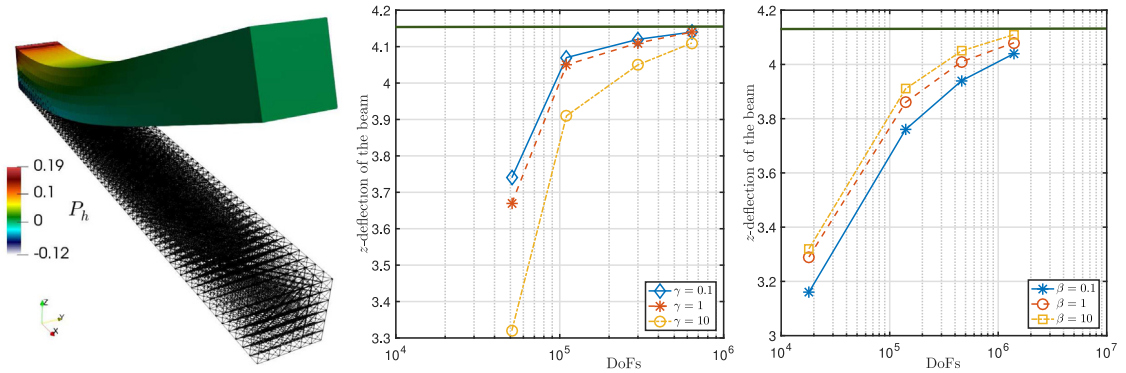

Fig. 5.4. Test 5. (a) deflection of the beam geometry with pressure distribution; (b) plot of deflection magnitudes at $(10, 0.5, 1)$ against the number of degrees of freedom (DoFs) for different values of γ at $\beta = 10$; (c) plot of deflection magnitudes at $(10, 0.5, 1)$ against the number of degrees of freedom (DoFs) for different values of β at $\gamma = 10$. The green horizontal line marks the reference value of 4.165 mm. (For interpretation of the references to colour in this figure legend, the reader is referred to the web version of this article.)

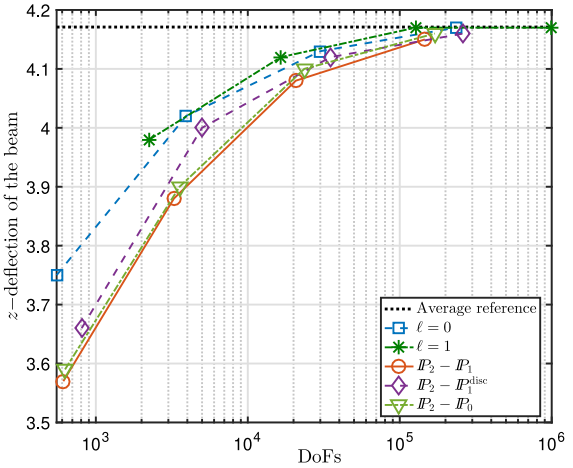

Fig. 5.5. Test 5. Deflection of the beam using the first and second order mixed Kirchhoff stress methods as well as three discretisations of the classical displacement–pressure formulation of hyperelasticity.

et al. [78]:

$$\Psi_{\text{GCM}} = a/2(e^Q - 1), \tag{5.1}$$

with $Q = b_f E_{ff}^2 + b_t(E_{ss}^2 + E_{nn}^2 + E_{sn}^2 + E_{ns}^2) + b_{fs}(E_{fs}^2 + E_{sf}^2 + E_{fn}^2 + E_{nf}^2)$, where $a = 2\,\text{kPa}$, $b_f = 8$, $b_t = 2$, $b_{fs} = 4$, and the E_{ij} denote entries of the Green–Lagrange strain tensor $\mathbf{E}$, rotated with respect to a local coordinate system aligned with $\boldsymbol{f}_0, \boldsymbol{s}_0, \boldsymbol{n}_0$.

The face $x = 0$ is fixed in all directions and a pressure of 0.004 kPa is applied to the bottom face $z = 0$. The z-coordinate of the end point $(10, 0.5, 1.0)$ after deflection, according to [35], is around 4.165 mm, consistent with the average of the values computed by the participants in the benchmark study [77].

Fig. 5.4 portrays the convergence in deflection magnitudes for different values of penalty parameter γ and pressure stabilisation constant β. The limits agree with the findings in [35,77] (where the green horizontal line marks the reference value), thus validating the accuracy of the discretisation and preconditioner. The performance of the preconditioner at different values of β and γ is illustrated in Tables 5.3–5.4.

Table 5.3
Test 5. Average number of Krylov iterations per Newton iteration at different values of β, fixing $\gamma = 10$.

# refinements	DoFs	Stabilisation constant (β)		
		0.1	1	10
1	1.8×10^4	3.55	2.95	2.50
2	1.4×10^5	3.86	2.86	2.45
3	4.6×10^5	3.96	2.86	2.73
4	1.4×10^6	4.29	3.14	2.73

Table 5.4
Test 5. Average number of Krylov iterations per Newton iteration at different values of γ, fixing $\beta = 10$, where NF denotes the convergence failure of the outer Newton solve. Increasing γ improves the approximation of the Schur complement and reduces the number of outer Krylov iterations, but makes the nonlinear problem more difficult to solve.

# refinements	DoFs	Penalty parameter (γ)			
		0.1	1	10	100
1	1.2×10^4	16.0	6.21	2.50	1.36
2	1.4×10^5	17.4	6.60	2.45	NF
3	4.6×10^5	18.0	7.20	2.73	NF
4	1.0×10^6	18.4	7.60	2.73	NF

Although the goal of this manuscript is not to compare a Kirchhoff stress formulation against other primal or mixed forms of hyperelasticity, for illustrative purposes we employ Test 5 to show the deflection obtained with classical displacement–pressure formulations using continuous and discontinuous pressures. Sparse direct solvers are employed in this case, and we set $\beta = 10$. Similarly as in Fig. 5.4(c), we display in the semi-log plot of Fig. 5.5 the outcome of the runs using the first and second order Kirchhoff stress methods together with the deflections produced by piecewise quadratic and continuous displacement approximations in combination with either affine and continuous pressure (Taylor–Hood elements), piecewise linear discontinuous pressures, and piecewise constant pressures. The figure shows that for a given number of degrees of freedom, the proposed schemes outperform the displacement–pressure methods. We also mention that for a given mesh partition, the memory usage and the associated CPU time required indicate that the lowest-order Kirchhoff stress method is more convenient than the $\mathbb{P}_2 - \mathbb{P}_1^{\text{disc}}$ scheme and only slightly more expensive than the other two displacement–pressure methods (while delivering higher accuracy).

The second problem (Test 6) considers the inflation of an ellipsoid-like geometry, simulating the deformation pattern of the left ventricle. As in Test 5, the constitutive relation (5.1) is adopted. The base plane $z = 5$ mm is fixed in all directions, and a pressure of 10 kPa is applied to the endocardial surface. Again by [35], the y-coordinate of the epicardial apex $(0, -23, 0)$ after inflation is around -28.8 mm.

We observe from Table 5.3 a slight decrease in the number of Krylov iterations as we increase the value of the stabilisation parameter, indicating that our preconditioner is robust to the pressure stabilisation employed. On the other hand, Table 5.4 illustrates a large decrease in the number of Krylov iterations as we increase γ. The failure of Newton solve is a direct consequence of the increasing nonlinearity of the problem as γ increases, as the constraint is nonlinear.

Table 5.5 allows us to see how the computational efficiency has improved after adopting the augmented Lagrangian preconditioner. We observe that at each mesh refinement, the average runtime after preconditioning is substantially reduced compared to that of solving the test problem using LU factorisation. We expect to see a larger amount of time saved for more complex simulations (i.e. as the number of degrees of freedom increases).

For Test 6, we observe from Fig. 5.6 the convergence in inflation magnitudes at the apex for different values of γ and β. Again, the limits agree with the results obtained in [35], thus validating the accuracy of the discretisation and preconditioner.

We observe from Table 5.6 a moderate decrease in the iteration count as we take larger stabilisation parameters, showing that the performance of the preconditioner is robust with respect to the pressure stabilisation employed.

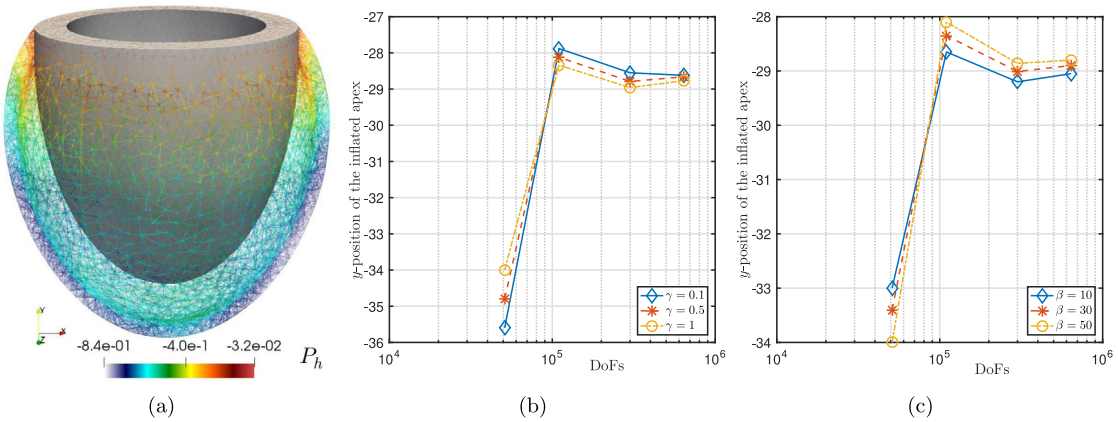

Fig. 5.6. Test 6. (a) inflation of the ellipsoid, pressure is shown by the colour bar; (b) plot of inflation magnitudes at epicardial apex (0, −23, 0) against the number of degrees of freedom (DoFs) for different values of γ at $\beta = 50$; (c) plot of inflation magnitudes at epicardial apex (0, −23, 0) against the number of degrees of freedom (DoFs) for different values of β at $\gamma = 1$. (For interpretation of the references to colour in this figure legend, the reader is referred to the web version of this article.)

Table 5.5
Test 5. Average runtime of solving the problem with LU factorisation (direct solver) applied to the full system, and using the augmented Lagrangian (AL) preconditioner with LU applied to the top-left block A, at $\beta = 10$ and $\gamma = 10$.

	Degrees of freedom (DoFs)		
	1.4×10^5	4.6×10^5	1.4×10^6
Direct solver for $\mathcal{A}$	3 min 09 s	24 min 07 s	3 h 12 min 02 s
AL preconditioner with direct solver for A	2 min 25 s	17 min 31 s	1 h 55 min 01 s
Speedup	1.30×	1.38×	1.67×

Table 5.6
Test 6. Average number of Krylov iterations per Newton iteration at different values of β, fixing $\gamma = 1$.

# refinements	DoFs	Stabilisation constant (β)		
		0.5	5	50
1	5.1×10^4	7.26	5.19	4.18
2	1.1×10^5	7.55	5.38	4.25
3	3.0×10^5	8.65	5.75	4.47
4	6.4×10^5	9.02	6.19	4.57

As in Test 5, Table 5.7 shows a considerable reduction in the number of Krylov iterations as we take larger values of γ.

Table 5.8 illustrates the average runtime of solving test 6 before and after the adoption of the augmented Lagrangian preconditioner at different mesh refinements. We observe that the computational efficiency of fine simulations is increased by roughly 10%–20% compared to that of applying LU factorisation to the whole system. As remarked at the end of Section 5.4, for cardiac electromechanics a much higher mesh resolution is required, and using solely direct solvers for $\mathcal{A}$ is ruled out.

Table 5.7
Test 6. Average number of Krylov iterations per Newton iteration at different values of γ, fixing $\beta = 5$.

# refinements	DoFs	Penalty parameter (γ)		
		0.1	1	10
1	5.1×10^4	14.7	5.19	2.47
2	1.1×10^5	15.4	5.38	2.51
3	3.0×10^5	16.6	5.75	2.58
4	6.4×10^5	17.2	6.19	2.66

Table 5.8
Test 6. Average runtime of solving the problem with LU factorisation (direct solver) applied to the full system, and using the augmented Lagrangian (AL) preconditioner with LU applied to the top-left block A, at $\beta = 50$ and $\gamma = 10$.

	Degrees of freedom (DoFs)		
	1.1×10^5	43.0×10^5	6.4×10^5
Direct solver for $\mathcal{A}$ (serial)	27 min 11 s	2 h 27 min 58 s	11 h 23 min 42 s
AL preconditioner with direct solver for A (serial)	24 min 32 s	2 h 10 min 58 s	9 h 59 min 5 s
Direct solver for $\mathcal{A}$ (8 cores)	6 min 41 s	34 min 16 s	2 h 37 min 0 s
AL preconditioner with direct solver for A (8 cores)	6 min 3 s	30 min 59 s	2 h 20 min 21 s
Direct solver for $\mathcal{A}$ (16 cores)	4 min 24 s	22 min 13 s	1 h 49 min 32 s
AL preconditioner with direct solver for A (16 cores)	4 min 22 s	19 min 51 s	1 h 29 min 59 s

6. Summary and concluding remarks

In this paper we have proposed an extension of a formulation for nonlinear hyperelasticity in the incompressible regime, which uses the Kirchhoff stress as one of the field variables. By recasting the continuous mixed problem in this way, the resulting formulation presents some advantages related to the straightforward imposition of stress symmetry, usability in recent models for stress-assisted diffusion, and discretisation using classical conforming polynomial spaces of arbitrary degree. We have discussed the solvability and stability of the linearised problem, and have proposed an augmented Lagrangian preconditioner. The use of exact Newton–Raphson Jacobians permits quadratic convergence to regular solutions in the nonlinear iterations. Several numerical examples have demonstrated the performance of the formulation and the robustness of the preconditioner in the solution of a number of benchmark problems and some tests arising in cardiac biomechanics. These methods are competitive when compared to classical displacement–pressure-based schemes. Nevertheless, further comparisons against other state-of-the-art stress-based methods should be conducted in future studies.

While the present family of methods exhibits appealing features as mentioned above, a drawback, shared with other stabilised methods for hyperelasticity (see, e.g., [28–30]), is that the stabilisation constant required for the lowest-order method needs to be chosen heuristically. For this we could explore different formulations using Kirchhoff stress, for instance applying integration by parts differently in the derivation of the variational formulation, and leading to divergence-conforming approximations of stress. This has been used successfully in a number of three-field formulations for linear elasticity using the Cauchy stress [21,25,79,80], but the principle is not straightforwardly carried over to the hyperelastic framework. Some formulations are available [3–5] in that context, but they consider the first Piola–Kirchhoff stress and displacement or adequate stress reconstructions from displacement and pressure [26]. In any case, also the preconditioning framework should be carefully restructured after changing the variational formulation.

Ongoing extensions of this work include the analysis of time-dependent formulations of hyperelasticity and understanding how the preconditioner should be adapted. We also plan to derive suitable a posteriori error estimators. Another important extension is the study of inner iterative solvers for the augmented Kirchhoff stress–displacement block in the preconditioner.

Generalising the analysis to include natural model extensions is also part of our goals, notably to the case of fully coupled electromechanics [24,31], as well as the introduction of contact and friction.

Declaration of competing interest

The authors declare that they have no known competing financial interests or personal relationships that could have appeared to influence the work reported in this paper.

Acknowledgements

We are grateful to Xiyao Li (Oxford MMSc programme) for her valuable contributions in the formulation and implementation of the numerical tests and many fruitful discussions regarding cardiac biomechanics. We also acknowledge the useful comments received from two anonymous referees, which resulted in substantial improvements to the presentation of the paper. This research has been supported by the Engineering and Physical Sciences Research Council, UK through the grants EP/R029423/1 and EP/V001493/1, by ANID-Chile through project Fondecyt 1181748, project Fondecyt 1200666 and project Centro de Modelamiento Matemático AFB 170001 of the PIA Program: Concurso Apoyo a Centros Científicos y Tecnológicos de Excelencia con Financiamiento Basal, Chile; by Universidad del Bío-Bío through project Grupo de Investigación 194608 GI/C; and by the HPC-Europa3 Transnational Access Grant HPC175QA9K.

References

[1] P. Wriggers, Nonlinear Finite Element Methods, Springer-Verlag, Berlin, 2008.
[2] D. Boffi, F. Brezzi, M. Fortin, Mixed Finite Element Methods and Applications, Springer-Verlag, Heidelberg, 2013.
[3] B. Müller, G. Starke, A. Schwarz, J. Schröder, A first-order system least squares method for hyperelasticity, SIAM J. Sci. Comput. 36 (5) (2014) B795–B816.
[4] R. Piltner, An alternative version of the Pian-Sumihara element with a simple extension to non-linear problems, Comput. Mech. 26 (2000) 483–489.
[5] N. Viebahn, J. Schröder, P. Wriggers, An extension of assumed stress finite elements to a general hyperelastic framework, Adv. Model. Simul. Eng. Sci. 6 (2019) e9.
[6] H. Kabaria, A.J. Lew, B. Cockburn, A hybridizable discontinuous Galerkin formulation for non-linear elasticity, Comput. Methods Appl. Mech. Engrg. 283 (2015) 303–329.
[7] M. Chiumenti, M. Cerevra, R. Codina, A mixed three-field FE formulation for stress accurate analysis including the incompressibility limit, Comput. Methods Appl. Mech. Engrg. 283 (2015) 1095–1116.
[8] H.R. Bayat, J. Krämer, L. Wunderlich, S. Wulfinghoff, S. Reese, B. Wohlmuth, C. Wieners, Numerical evaluation of discontinuous and nonconforming finite element methods in nonlinear solid mechanics, Comput. Mech. 62 (2018) 1413–1427.
[9] A. Schwarz, K. Steeger, M. Igelbüscher, J. Schröder, Different approaches for mixed LSFEMs in hyperelasticity: Application of logarithmic deformation measures, Internat. J. Numer. Methods Engrg. 115 (9) (2018) 1138–1153.
[10] J.H. Adler, L. Dorfmann, D. Han, S. MacLachlan, C. Paetsch, Mathematical and computational models of incompressible materials subject to shear, IMA J. Appl. Math. 79 (5) (2014) 889–914.
[11] U. Heisserer, S. Hartmann, A. Düster, Z. Yosibash, On volumetric locking-free behaviour of p-version finite elements under finite deformations, Commun. Numer. Methods Eng. 24 (11) (2007) 1019–1032.
[12] S. Reese, P. Wriggers, A stabilization technique to avoid hourglassing in finite elasticity, Internat. J. Numer. Methods Engrg. 48 (2000) 79–109.
[13] M. Fortin, M. Soulie, A non-conforming piecewise quadratic finite element on triangles, Internat. J. Numer. Methods Engrg. 19 (1983) 505–520.
[14] K.R. Srinivasan, K. Matouš, P.H. Geubelle, Generalized finite element method for modeling nearly incompressible bimaterial hyperelastic solids, Comput. Methods Appl. Mech. Engrg. 197 (2008) 4882–4893.
[15] J.C. Simo, R.L. Taylor, K.S. Pister, Variational and projection methods for the volume constraint in finite deformation elasto-plasticity, Comput. Methods Appl. Mech. Engrg. 51 (1985) 177–208.
[16] J.C. Simo, F. Armero, Geometrically non-linear enhanced strain mixed methods and the method of incompatible modes, Internat. J. Numer. Methods Engrg. 33 (1992) 1413–1449.
[17] J.C. Simo, R.L. Taylor, Quasi-incompressible finite elasticity in principal stretches. Continuum basis and numerical algorithms, Comput. Methods Appl. Mech. Engrg. 85 (3) (1991) 273–310.
[18] B.P. Lamichhane, E.P. Stephan, A symmetric mixed finite element method for nearly incompressible elasticity based on biorthogonal systems, Numer. Methods Partial Differential Equations 28 (4) (2012) 1336–1353.
[19] Y. Abdelaziz, A. Hamouine, A survey of the extended finite element, Comput. Struct. 86 (2008) 1141–1151.
[20] D.N. Arnold, Mixed finite element methods for elliptic problems, Comput. Methods Appl. Mech. Engrg. 82 (1–3) (1990) 281–300.
[21] G.N. Gatica, L.F. Gatica, E.P. Stephan, A dual-mixed finite element method for nonlinear incompressible elasticity with mixed boundary conditions, Comput. Methods Appl. Mech. Engrg. 196 (2007) 3348–3369.
[22] K.S. Chavan, B.P. Lamichhane, B.I. Wohlmuth, Locking-free finite element methods for linear and nonlinear elasticity in 2D and 3D, Comput. Methods Appl. Mech. Engrg. 196 (2007) 4075–4086.
[23] A. Propp, A. Gizzi, F. Levrero-Florencio, R. Ruiz-Baier, An orthotropic electro-viscoelastic model for the heart with stress-assisted diffusion, Biomech. Model. Mechanobiol. 19 (2) (2020) 633–659.

[24] R. Ruiz-Baier, A. Gizzi, A. Loppini, C. Cherubini, S. Filippi, Thermo-electric effects in an anisotropic active-strain electromechanical model, Commun. Comput. Phys. 27 (1) (2020) 87–115.
[25] D.N. Arnold, R.S. Falk, R. Winther, Mixed finite element methods for linear elasticity with weakly imposed symmetry, Math. Comp. 76 (2007) 1699–1723.
[26] F. Bertrand, M. Moldenhauer, G. Starke, Weakly symmetric stress equilibration for hyperelastic material models, GAMM-Mitt. 43 (2) (2020) 1–15.
[27] R. Ruiz-Baier, Primal-mixed formulations for reaction-diffusion systems on deforming domains, J. Comput. Phys. 299 (2015) 320–338.
[28] E. Karabelas, G. Haase, G. Plank, C.M. Augustin, Versatile stabilized finite element formulations for nearly and fully incompressible solid mechanics, Comput. Mech. 65 (2020) 193–215.
[29] G. Scovazzi, B. Carnes, X. Zeng, S. Rossi, A simple, stable, and accurate linear tetrahedral finite element for transient, nearly, and fully incompressible solid dynamics: A dynamic variational multiscale approach, Internat. J. Numer. Methods Engrg. 106 (10) (2016) 799–839.
[30] D. Baroli, A. Quarteroni, R. Ruiz-Baier, Convergence of a stabilized discontinuous Galerkin method for incompressible nonlinear elasticity, Adv. Comput. Math. 39 (2013) 425–443.
[31] F.S. Costabal, F.A. Concha, D.E. Hurtado, E. Kuhl, The importance of mechano-electrical feedback and inertia in cardiac electromechanics, Comput. Methods Appl. Mech. Engrg. 320 (2017) 352–368.
[32] S. Göktepe, S.N.S. Acharya, J. Wong, E. Kuhl, Computational modeling of passive myocardium, Int. J. Numer. Methods Biomed. Eng. 27 (2011) 1–12.
[33] M. Hadjicharalambous, J. Lee, N.P. Smith, D.A. Nordsletten, A displacement-based finite element formulation for incompressible and nearly-incompressible cardiac mechanics, Comput. Methods Appl. Mech. Engrg. 274 (2014) 213–236.
[34] J.A. Weiss, B.N. Maker, S. Govindjee, Finite element implementation of incompressible, traversely isotropic hyperelasticity, Comput. Methods Appl. Mech. Engrg. 135 (1996) 107–128.
[35] J.O. Campos, R. Weber dos Santos, J. Sundnes, B. Martins Rocha, Preconditioned augmented Lagrangian formulation for nearly incompressible cardiac mechanics, Int. J. Numer. Methods Biomed. Eng. 34 (4) (2018) e2948.
[36] J. Liu, A.L. Marsden, A robust and efficient iterative method for hyper-elastodynamics with nested block preconditioning, J. Comput. Phys. 383 (2019) 72–93.
[37] J. Whiteley, A preconditioner for the finite element computation of incompressible nonlinear elastic deformations, Comput. Mech. 60 (2017) 683–692.
[38] A.J. Wathen, Preconditioning, Acta Numer. 24 (2015) 329–376.
[39] M. Benzi, T. Miroslav, A sparse approximate inverse preconditioner for nonsymmetric linear systems, SIAM J. Sci. Comput. 19 (3) (1998) 968–994.
[40] M.F. Murphy, G.H. Golub, A.J. Wathen, A note on preconditioning for indefinite linear systems, SIAM J. Sci. Comput. 21 (2000) 1969–1972.
[41] M. Benzi, G.H. Golub, J. Liesen, Numerical solution of saddle point problems, Acta Numer. 14 (2005) 1–137.
[42] I.C.F. Ipsen, A note on preconditioning nonsymmetric matrices, SIAM J. Sci. Comput. 23 (2001) 1050–1051.
[43] H.C. Elman, D.J. Silvester, A.J. Wathen, Finite Elements and Fast Iterative Solvers: with Applications in Incompressible Fluid Dynamics, Oxford University Press, 2014.
[44] M. Benzi, M.A. Olshanskii, An augmented Lagrangian-based approach to the Oseen problem, SIAM J. Sci. Comput. 28 (6) (2006) 2095–2113.
[45] M. Fortin, R. Glowinski, Augmented Lagrangian Methods: Applications to the Numerical Solution of Boundary-Value Problems, Elsevier, 2000, p. 15.
[46] G.A. Holzapfel, R.W. Ogden, Constitutive modelling of passive myocardium: A structurally based framework for material characterization, Phil. Trans. R. Soc. A 367 (2009) 3445–3475.
[47] C. Mardare, A nonlinear Korn inequality with boundary conditions and its relation to the existence of minimizers in nonlinear elasticity, C. R. Math. 349 (3–4) (2011) 229–232.
[48] P.G. Ciarlet, Mathematical Elasticity Vol. 1: Three-Dimensional Elasticity, North Holland, Amsterdam, 1988.
[49] T. Valent, Boundary Value Problems of Finite Elasticity: Local Theorems on Existence, Uniqueness, and Analytic Dependence on Data, Springer-Verlag, 1988.
[50] J.C. Bellido, J. Cueto, C. Mora-Corral, Nonlocal hyperelasticity and polyconvexity in fractional spaces, arXiv preprint, 2018, 1812.05848.
[51] J.M. Ball, Singularities and computation of minimizers for variational problems, Found. Comput. Math. 284 (1999) 1–20.
[52] J.M. Ball, F. Murat, $W^{1,p}$-Quasiconvexity and variational problems for multiple integrals, J. Funct. Anal. 58 (1984) 225–253.
[53] E. Stein, M. Rüter, Finite element methods for elasticity with error-controlled discretization and model adaptivity, in: E. Stein, R. de Borst, T. Hughes (Eds.), Encyclopedia of Computational Mechanics, Wiley, 2004, pp. 5–58.
[54] J.M. Ball, Convexity conditions and existence theorems in nonlinear elasticity, Arch. Ration. Mech. Anal. 63 (1977) 337–403.
[55] K. Zhang, Energy minimizers in nonlinear elastostatics and the implicit function theorem, Arch. Ration. Mech. Anal. 114 (1991) 95–117.
[56] P. Le Tallec, Existence and approximation results for nonlinear mixed problems: Application to incompressible finite elasticity, Numer. Math. 38 (1982) 365–382.
[57] G.N. Gatica, A Simple Introduction to the Mixed Finite Element Method. Theory and Applications, in: Springer Briefs in Mathematics, Springer, Cham Heidelberg New York Dordrecht London, 2014.
[58] V. Girault, P.A. Raviart, Finite Element Methods for Navier-Stokes Equations. Theory and Algorithms, in: Springer Series in Computational Mathematics, vol. 5, Springer-Verlag, Berlin, 1986.

[59] S.C. Brenner, L.R. Scott, The Mathematical Theory of Finite Element Methods, third ed., in: Texts in Applied Mathematics, vol. 15, Springer, New York, 2008.
[60] P.E. Farrell, L. Mitchell, F. Wechsung, An augmented Lagrangian preconditioner for the 3D stationary incompressible Navier-Stokes equations at high Reynolds number, SIAM J. Sci. Comput. 41 (5) (2019) A3073–A3096.
[61] C. Bacuta, A unified approach for Uzawa algorithms, SIAM J. Numer. Anal. 44 (6) (2006) 2633–2649.
[62] P.E. Farrell, P.A. Gazca-Orozco, An augmented Lagrangian preconditioner for implicitly-constituted non-Newtonian incompressible flow, SIAM J. Sci. Comput. 42 (6) (2020) B1329–B1349.
[63] V.T. Polyak, N.V. Tret'yakov, The method of penalty estimates for conditional extremum problems, USSR Comput. Math. Math. Phys. 13 (1974) 42–58.
[64] Y. Saad, A flexible inner-outer preconditioned GMRES algorithm, SIAM J. Sci. Comput. 14 (1992) 461–469.
[65] J. Schöberl, Multigrid methods for a parameter dependent problem in primal variables, Numer. Math. 84 (1) (1999) 97–119.
[66] M.S. Alnæs, J. Blechta, J. Hake, A. Johansson, B. Kehlet, A. Logg, C. Richardson, J. Ring, M.E. Rognes, G.N. Wells, The FEniCS project version 1.5, Arch. Numer. Softw. 3 (100) (2015) 9–23.
[67] F. Rathgeber, D.A. Ham, L. Mitchell, M. Lange, F. Luporini, A.T.T. McRae, G.-T. Bercea, G.R. Markall, P.H.J. Kelly, Firedrake: Automating the finite element method by composing abstractions, ACM Trans. Math. Software 43 (3) (2017) 24.
[68] G. Balaban, M.S. Alnæes, J. Sundnes, M.E. Rognes, Adjoint multi-start-based estimation of cardiac hyperelastic material parameters using shear data, Biomech. Model. Mechanobiol. 15 (6) (2016) 1509–1521.
[69] M.H.G. Heusinkveld, S. Quicken, R.J. Holtackers, W. Huberts, K.D. Reesink, T. Delhaas, B. Spronck, Uncertainty quantification and sensitivity analysis of an arterial wall mechanics model for evaluation of vascular drug therapies, Biomech. Model. Mechanobiol. 17 (8) (2018) 55–69.
[70] S. Gjerald, J. Hake, S. Pezzuto, J. Sundnes, S.T. Wall, Patient-specific parameter estimation for a transversely isotropic active strain model of left ventricular mechanics, in: O. Camara, T. Mansi, M. Pop, M. Rhode, M. Sermesant, A. Young (Eds.), Statistical Atlases and Computational Models of the Heart-Imaging and Modelling Challenges, Springer, Berlin, 2015.
[71] H. Wang, H. Gao, X. Luo, Structure-based finite strain modelling of the human left ventricle in diastole, Int. J. Numer. Methods Biomed. Eng. 29 (2013) 83–103.
[72] S. Reese, On the equivalence of mixed element formulations and the concept of reduced integration in large deformation problems, Int. J. Nonlinear Sci. Numer. Simul. 3 (2002) 1–33.
[73] J.D. Bayer, R.C. Blake, G. Plank, N.A. Trayanova, A novel rule-based algorithm for assigning myocardial fiber orientation to computational heart models, Ann. Biomed. Eng. 40 (10) (2012) 2243–2254.
[74] J. Wong, E. Kuhl, Generating fiber orientation maps in human heart models using Poisson interpolation, Comput. Methods Biomech. Biomed. Eng. 11 (2014) 1217–1226.
[75] L. Barbarotta, S. Rossi, L. Dede, A. Quarteroni, A transmurally heterogeneous orthotropic activation model for ventricular contraction and its numerical validation, Int. J. Numer. Methods Biomed. Eng. 34 (2) (2018) e3137.
[76] S. Rossi, T. Lassila, R. Ruiz-Baier, A. Sequeira, A. Quarteroni, Thermodynamically consistent orthotropic activation model capturing ventricular systolic wall thickening in cardiac electromechanics, Eur. J. Mech. A Solids 48 (2014) 129–142.
[77] S. Land, et al., Verification of cardiac mechanics software: Benchmark problems and solutions for testing active and passive material behaviour, Proc. R. Soc. A. 471 (2184) (2015) 20150641.
[78] J.M. Guccione, K.D. Costa, A.D. McCulloch, Finite element stress analysis of left ventricular mechanics in the beating dog heart, J. Biomech. 28 (1995) 1167–1177.
[79] A. Klawonn, G. Starke, A preconditioner for the equations of linear elasticity discretized by the PEERS element, Numer. Linear Algebra Appl. 11 (2004) 1–16.
[80] B.P. Lamichhane, B. Reddy, B. Wohlmuth, Convergence in the incompressible limit of finite element approximations based on the Hu–Washizu formulation, Numer. Math. 104 (2006) 151–175.